

## THE $\nu$ PROCESS IN THE LIGHT OF AN IMPROVED UNDERSTANDING OF SUPERNOVA NEUTRINO SPECTRA

A. SIEVERDING<sup>1,2</sup>, G. MARTÍNEZ-PINEDO<sup>2,1</sup>, L. HUTHER<sup>1</sup>, K. LANGANKE<sup>2,1</sup>, AND A. HEGER<sup>3,4,5</sup>

<sup>1</sup>Institut für Kernphysik (Theoriezentrum), Technische Universität Darmstadt, Schlossgartenstraße 2, 64289 Darmstadt, Germany

<sup>2</sup>GSI Helmholtzzentrum für Schwerionenforschung, Planckstraße 1, 64291 Darmstadt, Germany

<sup>3</sup>Monash Centre for Astrophysics, School of Physics and Astronomy, Monash University, Victoria 3800, Australia

<sup>4</sup>Tsung-Dao Lee Institute, Shanghai 200240, China and

<sup>5</sup>The Joint Institute for Nuclear Astrophysics, Michigan State University, East Lansing, Michigan 48824, USA

*Draft version May 28, 2018*

### ABSTRACT

We study the neutrino-induced production of nuclides in explosive supernova nucleosynthesis for progenitor stars with solar metallicity including neutrino nucleus reactions for all nuclei with charge numbers  $Z < 76$  with average neutrino energies in agreement with modern Supernova simulations. Considering progenitors with initial main sequence masses between  $13 M_{\odot}$  and  $30 M_{\odot}$ , we find a significant production of  $^{11}\text{B}$ ,  $^{138}\text{La}$ , and  $^{180}\text{Ta}$  by neutrino nucleosynthesis, despite the significantly reduced neutrino energies. The production of  $^{19}\text{F}$  turns out to be more sensitive to the progenitor mass and structure than to the  $\nu$  process. With our complete set of cross sections we have identified effects of the  $\nu$  process on several stable nuclei including  $^{33}\text{S}$ ,  $^{40}\text{Ar}$ ,  $^{41}\text{K}$ ,  $^{59}\text{Co}$ , and  $^{113}\text{In}$  at the 10% level. Neutrino-induced reactions contribute to a similar extent to the production of radioactive  $^{26}\text{Al}$  and increase the yield of  $^{22}\text{Na}$  by 50%. Future  $\gamma$  ray astronomy missions may reach the precision at which the contribution from the  $\nu$  process becomes relevant. We find that the production of  $^{22}\text{Na}$  by the  $\nu$  process could explain the Ne-E(L) component of meteoritic graphite grains. The  $\nu$  process enhances the yield of  $^{36}\text{Cl}$  and we point out that the resulting  $^{36}\text{Cl}/^{35}\text{Cl}$  ratio is in agreement with the values inferred for the early solar system. Our extended set of neutrino-nucleus interactions also allows us to exclude any further effects of the  $\nu$  process on stable nuclei and to quantify the effects on numerous, hitherto unconsidered radioactive nuclei, e.g.,  $^{36}\text{Cl}$ ,  $^{72}\text{As}$ ,  $^{84}\text{Rb}$ , and  $^{88}\text{Y}$ .

### 1. INTRODUCTION

Astrophysical objects like stars, novae, or supernovae are the origin of most of the elements in the Universe (Burbidge et al. 1957; Cameron 1957). Whereas the likely nucleosynthesis processes associated with these objects have been identified and a general understanding has been developed, many details of their operation are still unresolved (Wiescher et al. 2012; Thielemann et al. 2011; Arnould & Takahashi 1999). This is due to limited computational capabilities to simulate astrophysical objects and the full range of their varieties and to the fact that the properties of the nuclides involved in the nucleosynthesis processes are not known experimentally and have to be modeled (Grawe et al. 2007; Langanke & Schatz 2013).

An important test for models that aim to describe how the elements are formed is the reproduction the chemical composition of well-known objects like the Solar System. The composition of the Solar System has been determined with high accuracy (Lodders 2003; Asplund et al. 2009) but we still lack the full understanding of the origin of all the isotopes that can be observed since it likely involves contributions from a multitude of events that are difficult to disentangle. Primitive meteorites are another source of information on the nucleosynthesis that has contributed to the composition of our solar system. Isotopic anomalies have allowed to prescribe pre-solar grains that reflect the composition of the early solar system (ESS) to different astrophysical scenarios. The presence of  $^{44}\text{Ti}$  and an excess of Si as well as the isotopic ratios of Fe and Ni in SiC-X grains and graphite grains have led to the conclusion that these grains originate from a core-collapse supernova (Amari et al. 1992). Detections of gamma-rays from radioactive nuclei by space bound observatories like INTE-

GRAL (Winkler et al. 2011) are another invaluable tool to determine sites of active nucleosynthesis and thereby advance our understanding of astrophysical nucleosynthesis. Such detection allows for a snapshot view of the ongoing nucleosynthesis in our galaxy and, provided a suited nuclear half-life, to relate the origin of the nuclide to a specific astrophysical source (Diehl et al. 2006). In cases where the observation can be assigned to a particular supernova remnant, one can learn about asymmetries in the explosion (Grefenstette et al. 2014; Wongwathanarat et al. 2017). The prime nuclide for gamma-ray astronomy in recent years has been  $^{26}\text{Al}$  (Diehl 2013). Its production has been associated with several astrophysical sources (see Woosley et al. 1990, and references therein), however, in recent years evidence has been brought forward (Timmes et al. 1995; Diehl & Timmes 1998; Diehl 2013) that massive stars can account for most of the  $^{26}\text{Al}$  in the galaxy. Other gamma-ray astronomy candidates such as  $^{22}\text{Na}$ ,  $^{44}\text{Ti}$ , and  $^{60}\text{Fe}$  are also related to core-collapse supernovae (Iyudin et al. 1994; Timmes et al. 1995; Woosley et al. 2002; Rauscher et al. 2002; Limongi & Chieffi 2006).

It has long been recognized that neutrino-nucleus reactions are essential for the synthesis of selected nuclides including  $^7\text{Li}$ ,  $^{11}\text{B}$ ,  $^{15}\text{N}$ ,  $^{19}\text{F}$ ,  $^{138}\text{La}$ , and  $^{180}\text{Ta}$  (Woosley et al. 1990; Heger et al. 2005) or can contribute to the production of long-lived radioactive nuclides (Woosley et al. 1990; Timmes et al. 1995; Woosley et al. 2002; Rauscher et al. 2002). This is denoted as  $\nu$  process and involves neutrinos of all flavors, which emitted from the hot proto-neutron star (PNS) formed after a supernova explosion, interact with nuclei as they pass through the surrounding stellar matter. At the same time, these outer layers are heated up and compressed by the explosion shock-wave propagating outward from the PNS and causing the ejec-

tion of the material. Neutral-current reactions excite the nucleus to states above particle thresholds so that the subsequent decay is accompanied by emission of light particles (proton, neutron, or  $\alpha$  particle). Due to the relatively low energies of the neutrinos, charged-current reactions can only be induced by electron-type neutrinos. This process can be accompanied by light-particle emission if the  $(\nu_e, e^-)$  or  $(\bar{\nu}_e, e^+)$  reactions excite the daughter nucleus to levels above particle thresholds. Hence there are two possible ways for the  $\nu$  process to contribute to nucleosynthesis. Firstly, rare nuclei, e.g.,  $^{11}\text{B}$ ,  $^{19}\text{F}$ ,  $^{138}\text{La}$ , and  $^{180}\text{Ta}$ , can be produced directly as daughter products of neutrino-induced reactions on abundant nuclei. And secondly, neutrino spallation reactions increase the amount of light particles required to synthesize some nuclides such as  $^7\text{Li}$  and  $^{26}\text{Al}$  within a network of charged-particle reactions.

The focus of this article is to review the  $\nu$  process in the light of an improved understanding of neutrino properties in core-collapse supernovae and with an improved set of neutrino-nucleus cross sections covering all nuclei in the reaction network to explore in particular the impact of the  $\nu$  process on the production of long-lived radioactive nuclei of interest to gamma-ray astronomy. Previous investigations of nucleosynthesis by neutrino-induced reactions have been based on stellar simulations using various hydrodynamical models (Woosley et al. 1990; Heger et al. 2005; Limongi & Chieffi 2006) and neutrino-nucleus cross section data which were restricted to a set of key nuclei, especially those which are quite abundant in outer burning shells, and to a limited number of decay channels. Furthermore, the simulations adopted supernova neutrino energy spectra, described by Fermi-Dirac distributions with chemical potential  $\mu = 0$  and temperature  $T_\nu$ , which were appropriate at the time the studies were performed. They used  $T_{\nu_e, \bar{\nu}_e} = 4\text{--}5$  MeV for electron (anti)neutrinos, corresponding to average energies,  $\langle E_\nu \rangle = 3.15 T_\nu$ , between 12 MeV and 16 MeV (Woosley et al. 1990; Heger et al. 2005) and  $T_{\nu_\mu, \tau} = 5\text{--}10$  MeV (Woosley et al. 1990; Timmes et al. 1995; Heger et al. 2005) for muon and tau neutrinos as well as for the corresponding anti-neutrinos, corresponding to average energies between 16 MeV and 32 MeV.

We improve these simulations in two relevant aspects. Firstly, we have derived a complete set of partial differential cross sections for neutrino-induced charged- and neutral-current reactions for nuclei with charge numbers  $Z < 76$  considering various single- and multi-particle decay channels. For several key reactions, we have derived the cross sections either directly from experimental data or from shell model calculations which is the most accurate theoretical tool to describe low-energy neutrino-nucleus reactions (Langanke & Martínez-Pinedo 2003; Balasi et al. 2015). The relevant cross sections are provided in the supplemental material. Secondly, the more realistic treatment of neutrino transport in recent supernova simulations (Fischer et al. 2010; Hüdepohl et al. 2010; Martínez-Pinedo et al. 2012; Martínez-Pinedo et al. 2014; Mirizzi et al. 2016) yield spectra for all neutrino families which are noticeably shifted to lower energies. This reduces the neutrino-nucleus cross sections and in particular particle spallation cross sections for neutral-current reactions which are very sensitive to the tail of the neutrino spectra due to the relatively high particle separation thresholds involved. Our choice of neutrino temperatures denoted “low energies” is  $T_{\nu_e} = 2.8$  MeV ( $\langle E_{\nu_e} \rangle = 9$  MeV),  $T_{\bar{\nu}_e, \nu_\mu, \tau} = 4$  MeV ( $\langle E_{\bar{\nu}_e, \nu_\mu, \tau} \rangle = 12$  MeV), in agreement with recent simulations (Hüdepohl et al. 2010; Martínez-Pinedo et al. 2012;

Martínez-Pinedo et al. 2014; Mirizzi et al. 2016). To compare with previous neutrino nucleosynthesis studies (Woosley et al. 1990; Heger et al. 2005) we have also performed our calculations using the following set of neutrino temperatures:  $T_{\nu_e} = 4$  MeV ( $\langle E_{\nu_e} \rangle = 12$  MeV),  $T_{\bar{\nu}_e} = 5$  MeV ( $\langle E_{\bar{\nu}_e} \rangle = 15.8$  MeV), and  $T_{\nu_\mu, \tau} = 6.0$  MeV ( $\langle E_{\nu_\mu, \tau} \rangle = 19$  MeV); that we denote as “high energies” along the manuscript.

The paper is organized as follows: In §2 we discuss our calculations of neutrino-nucleus reactions with a particular focus on the cases for which experimental data are available. After a brief description of the supernova model in §3, we discuss our results for the stable nuclei in §4 and then the impact on radioactive nuclei in §5. Finally, we conclude in §6.

## 2. NEUTRINO-NUCLEUS CROSS SECTIONS

We have calculated partial differential neutrino-nucleus cross sections globally for nuclei with  $Z < 76$  based on a two-step strategy (Kolbe et al. 1992): *i*) the neutrino-induced nuclear excitation cross sections to a final state at energy  $E$  have been calculated within the Random Phase Approximation following Kolbe et al. (2003) and considering multipole transitions up to order four. The single particle energies were adopted from an appropriate Woods-Saxon parametrization, adjusted to reproduce the proton and neutron thresholds and to account for the energies of the Isobaric Analog State and the leading giant resonances. *ii*) The decay probabilities of the excited nuclear levels have been derived within the statistical model. At low excitation energies we use the Modified Smoker code (Loens 2010) which considers experimentally known states and their properties explicitly and then matches the experimental spectrum to a level density. The code is restricted to treat single-particle decays. To allow for multi-particle decay, which becomes relevant at modest excitation energies or in nuclei with large neutron excess and hence small separation energies, we have adopted the ABLA code (Kelić et al. 2009) at higher excitation energies, which has been validated to properly describe multi-particle decays and fission. The results of the two statistical model codes have been smoothly matched at moderate energies above the single-particle thresholds.

Using cross sections for neutrino nucleus reactions based on Random Phase Approximation (RPA) is justified by the relatively high energy of incoming neutrinos that are large compared to the energy scale of nuclear excitations. In this case collective excitations dominate and in RPA the centroid of the strength of collective excitations are reproduced quite reliably without the need of a precise reproduction of the detailed fragmentation.

A particular relevant nucleus for gamma-ray astronomy is  $^{26}\text{Al}$  that is produced in the  $\nu$  process by the reaction  $^{26}\text{Mg}(\nu_e, e^-)^{26}\text{Al}$  and will be discussed in detail in §5. This reaction has been considered previously by Domogatskii & Nadezhin (1980) where the cross section was estimated considering the Fermi contribution to the isobaric analog state and Gamow-Teller transitions from the  $\beta^+$  decay of  $^{26}\text{Si}$ , the mirror nucleus to  $^{26}\text{Mg}$ . Zegers et al. (2006) have extracted the B(GT) strength distribution based on  $^{26}\text{Mg}(^3\text{He}, t)$  charge exchange reactions with high resolution. This has the advantage of not having the energy limitations of beta-decay and allows to determine transitions to all relevant states in  $^{26}\text{Al}$ . Based on these data and the known Fermi transition to the isobaric analog state we have calculated the cross sections for  $^{26}\text{Mg}(\nu_e, e^-)^{26}\text{Al}$ . In order to account for additional contribu-

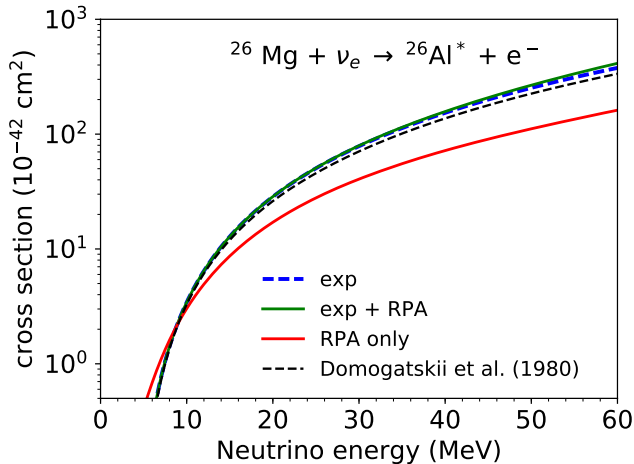


**Figure 1.** Cross section for the reaction  $^{26}\text{Mg}(\nu_e, e^-)^{26}\text{Al}$  based on the experimentally determined strength only (exp) and also with additional strength from calculated transitions at higher energies (exp + RPA). For comparison the theoretical results based on RPA and the estimate of Domogatskii & Nadezhin (1980) are also shown.

tions from forbidden transitions relevant at high neutrino energies, the cross section has been supplemented by RPA calculations. As can be seen in Figure 1, the contribution to the cross section from forbidden transitions is rather small. Also shown is the estimate of Domogatskii & Nadezhin (1980) and the purely theoretical RPA cross section. With appropriate quenching factors RPA calculation have been shown to give good estimates for the for the centroid of the B(GT) strength and to fulfill sum rules. It does not reproduce the fragmentation of the distribution very well (Kolbe et al. 2003; Balasi et al. 2015) which is important for reactions on intermediate mass nuclei at low energies that are dominated by a few individual transitions. The charged-current reaction  $^{26}\text{Mg}(\nu_e, e^-)^{26}\text{Al}$  is particularly difficult to treat in the RPA because it is sensitive to the distribution of the strength at low energies. Furthermore, for nuclei that are close to  $N = Z$  the Gamow-Teller strength is not determined by the Ikeda sum rule as it is the case of nuclei with moderate and large neutron excess. Figure 1 also shows the cross sections based on the RPA calculations and we find that it is 60% smaller than the one based on data for the relevant neutrino energies. This discrepancy exceeds the typical uncertainty that are expected from RPA neutrino cross section calculations (Balasi et al. 2015). For neutral-current interactions only reactions that lead to particle emission are relevant for nucleosynthesis and electron antineutrinos are expected to have higher energies. For such reactions, collective excitations at higher energies become more relevant and the cross sections are less sensitive to the details of the strength distribution. Therefore, we expect the values for such reactions to be even more accurate. Caurier et al. (1999) and others have shown that the shell model can describe the details of the B(GT) strength distribution with high accuracy (see also Balasi et al. 2015). We use results from such calculations wherever available.

The radioactive nucleus  $^{36}\text{Cl}$  is of some particular interest because it has been found in material from the early solar system (Murty et al. 1997). The reaction  $^{36}\text{S}(\nu_e, e^-)^{36}\text{Cl}$  can contribute to the production of  $^{36}\text{Cl}$  in supernovae. We have determined the cross section by combining the data from the mirror  $\beta^+$  decay of  $^{36}\text{Ca}$  and Gamow-Teller strength determined by shell-model calculations using the USDB interac-

tion (Brown & Richter 2006) with forbidden contributions determined from the RPA calculations. A secondary production channel for the production of  $^{36}\text{Cl}$  is provided by the reaction  $^{36}\text{Ar}(\bar{\nu}_e, e^-)^{36}\text{Cl}$  that we have determined by combining shell-model calculations for the Gamow-Teller strength and RPA for the forbidden transitions.

The reaction  $^{22}\text{Ne}(\nu_e, e^-)^{22}\text{Na}$  is relevant for the production of the radioactive isotope  $^{22}\text{Na}$  and has been determined by using data from the  $\beta^+$  decay of the mirror nucleus  $^{22}\text{Mg}$  combined with shell-model calculations for the Gamow-Teller strength and RPA calculations for the forbidden strength.

Other relevant cross sections are taken from the literature. Cross-sections for  $^4\text{He}$  are taken from Gazit & Barnea (2007). For  $^{12}\text{C}(\nu, \nu' ^3\text{He})^9\text{Be}$ ,  $^{12}\text{C}(\nu, \nu' ^4\text{He} ^3\text{H p})^4\text{He}$ , and  $^{12}\text{C}(\nu, \nu' ^4\text{He} ^3\text{He n})^4\text{He}$  the values used by Woosley et al. (1990) are adopted. One and two proton and neutron emission from  $^{12}\text{C}$ ,  $^{14}\text{N}$ ,  $^{16,18}\text{O}$ ,  $^{20,22}\text{Ne}$ ,  $^{24,26}\text{Mg}$ , and  $^{26,28}\text{Si}$  follow the approach discussed by Heger et al. (2005). The cross sections on  $^{20}\text{Ne}$  is based on charge-exchange data (Anderson et al. 1991) now extended to both neutral-current and charged-current cross sections. Cross sections for  $\nu_e$  absorption on  $^{138}\text{Ba}$  and  $^{180}\text{Hf}$  are based on measured Gamow-Teller strengths (Byelikov et al. 2007) with branching ratios for particle emission based on a statistical model (Loens 2010).

In addition to the updated  $\nu$ -induced reaction rates our work includes recent updates of thermonuclear reactions rates, in particular proton-, neutron- and alpha capture rates as contained in the most recent release of the JINA REACLIB reaction rate library, Version 2.2 (Cyburt et al. 2010) which contains important improvements for example on proton induced reactions (Iliadis et al. 2001) and neutron capture rates (Dillmann et al. 2014). Neutron capture rates are particularly important to determine the final abundances of  $^{138}\text{La}$  and  $^{180}\text{Ta}$ . While we use the updated rates from KADoNiS v0.3 for  $^{179,180}\text{Ta}(n, \gamma)$ , we revert to the values by Rauscher & Thielemann (2000) for  $^{137,138}\text{La}(n, \gamma)$  for reasons of consistency as explained in §4.3.

### 3. SUPERNOVA MODEL AND NUCLEAR REACTION NETWORK

The  $\nu$  process operates before, during and after the shock wave reaches the different regions of the star. The evolution of the shock-wave passing through the outer layers of the star is calculated using the implicit hydrodynamics package KEPLER (Weaver et al. 1978; Woosley & Weaver 1995; Woosley et al. 2002). In this framework, the explosion is driven by a piston that is positioned at the edge of the Fe core and the trajectory of the piston is adjusted to achieve an explosion energy of  $1.2 \times 10^{51}$  erg for all the models we have computed. We use supernova progenitors from a set that has been evolved in the same numerical framework as discussed by Rauscher et al. (2002), spanning initial masses between 13-30  $M_{\odot}$ . It is unclear which of the explored models would explode self-consistently and how the explosion energy and amount of fallback depend on progenitor mass and structure (Woosley & Weaver 1995; Horiuchi et al. 2014; Sukhbold & Woosley 2014; Ertl et al. 2016). Taking the same explosion energy for all the models probably also affects the systematics with respect to the progenitor mass. The progenitor-explosion connection, however, is still an open question and active field of research (Müller et al. 2016; Sukhbold et al. 2017).

The progenitor models we study here have been affected by the coding error affecting the neutrino loss rates reported

by Sukhbold et al. (2017) that affect the progenitor structure, in particular the innermost regions. However, the  $\nu$  process operates mostly regions beyond the O/Ne shell which we are not significantly affected by this error.

Since our results are based on one-dimensional calculations the results depend on the choice of the mass cut, which determines the amount of the material that is accreted onto the central object (fallback) and determines how much of the innermost part of the star can be successfully ejected by the explosion. Since the  $\nu$  process mainly operates in outer regions of the stellar mantle the results should not be affected significantly by fallback. Nevertheless, fallback may trigger the formation of a black hole resulting in a sudden end of neutrino emission (Fischer et al. 2009). This possibility is neglected in our calculations.

For the sake of comparison with previous studies and since neutrino energies and luminosities from self-consistent explosion simulations are still rare and the quantitative relations to the progenitor model are not established yet (Müller et al. 2016; Sukhbold et al. 2017) we model the neutrino emission with a exponentially decreasing luminosity  $L_\nu = L_0 \exp(-t/\tau_\nu)$  with  $\tau_\nu = 3$  s and  $L_0$  chosen to result in a total energy of  $3 \times 10^{53}$  erg emitted as neutrinos and distributed equally over the six neutrino flavors. Abundances are evolved using a nuclear reaction network including 1988 species up to  $2.5 \times 10^4$  s after bounce when the most short-lived nuclei have already decayed and those potentially interesting for observations remain. If not stated otherwise, mass fractions of radioactive nuclei quoted here have been extracted at this time. Nuclear reactions are switched off, once the temperature drops below  $10^7$  K. However beta-decays and neutrino reactions are followed till the end of the calculation. The size of the nuclear reaction network matches the co-processing network that was employed in the calculations of the stellar evolution of the progenitor models (Woosley et al. 2002). Therefore, any effects from the  $s$  process during stellar evolution are included. This is particularly important for the nucleosynthesis of the heaviest species:  $^{92}\text{Nb}$ ,  $^{98}\text{Tc}$ ,  $^{138}\text{La}$  and  $^{180}\text{Ta}$ .

#### 4. STABLE ISOTOPES

The typical nuclei that are sensitive to neutrino nucleosynthesis are  $^7\text{Li}$ ,  $^{11}\text{B}$ ,  $^{15}\text{N}$ ,  $^{19}\text{F}$ ,  $^{138}\text{La}$ , and  $^{180}\text{Ta}$  (Woosley et al. 1990; Heger et al. 2005), all of which are observed in the solar system, but are not produced in sufficient amount by nucleosynthesis calculations without including neutrino interactions. Neutrino nucleosynthesis pushes the averaged production factors of those nuclei closer to the solar system values. Table 1 shows the production factors relative to  $^{16}\text{O}$  averaged over our set of progenitors weighted with a Salpeter initial mass function (IMF) with  $dN_*/dm_* \propto m_*^{-1.35}$ . The production factor for a species  $A$  is defined as  $P_A = (X_A^*/X_A^\odot)/(X_{^{16}\text{O}}^*/X_{^{16}\text{O}}^\odot)$ . We find that due to the reduction of the  $\nu$  energies the effect of the  $\nu$  process is diminished which solves the problem of the slight overproduction of  $^{11}\text{B}$ .

Figure 2 shows the dependence of the total yields of the five  $\nu$ -process isotopes shown in Table 1 on the initial mass of the stellar model. Stellar structure affects the  $\nu$  process by three major aspects. Firstly, as a secondary process the  $\nu$  process predominantly operates on abundant seed nuclei and the composition therefore determines where the process can occur. Secondly, the stellar density and temperature profiles determines how strong the supernova shock affects the regions where the  $\nu$  process seeds are located. Finally, the stellar

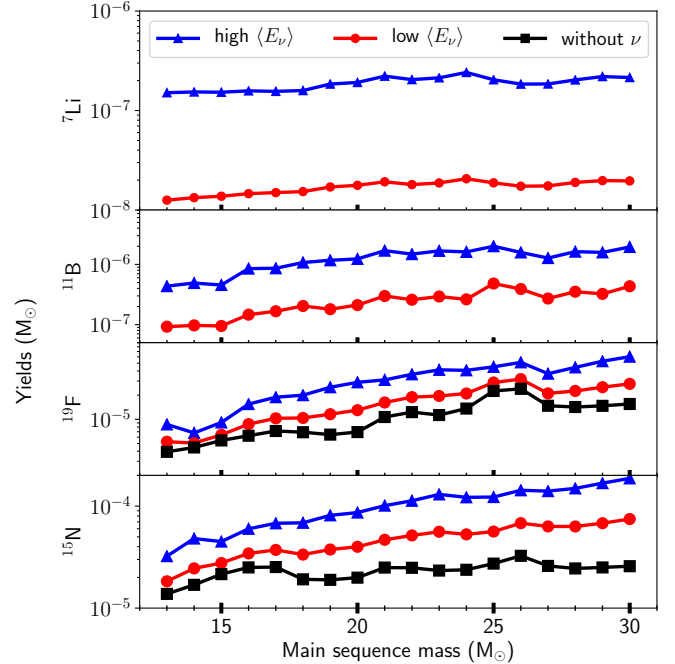


**Figure 2.** Total yields for the nuclei with largest contributions from the  $\nu$  process for the range of progenitors studied here. Averaged production factors are summarized in Table 1. Note that the scale of the y axis is different for each panel. The production of  $^7\text{Li}$  and  $^{11}\text{B}$  without neutrinos is negligible and not shown in the figure.

model determines the distance of the regions of interest from the proto-neutron star and hence the intensity of the neutrino fluxes.

Due to the complex interplay of nuclear burning, convection and hydrostatic adjustment that governs stellar evolution monotonous trends with respect to the initial mass are not expected. Still, Figure 2 shows that the relative enhancement for the  $\nu$ -process nuclei and in particular for the light elements Li and B are quite robust with respect to the progenitor. In general, the  $\nu$ -process contributions tend to have a smoothing effect on variations with initial mass which we also find for the radioactive nuclei discussed in §5. In the following we will discuss the production of  $^7\text{Li}$ ,  $^{11}\text{B}$ ,  $^{19}\text{F}$ ,  $^{15}\text{N}$ ,  $^{138}\text{La}$  and  $^{180}\text{Ta}$  in more detail.

##### 4.1. The light nuclei $^7\text{Li}$ and $^{11}\text{B}$

The light elements  $^7\text{Li}$  and  $^{11}\text{B}$  are present in the solar system with abundances of  $1.5 \times 10^{-9}$  and  $4 \times 10^{-10}$  (Lodders 2003). Since these nuclei are easily destroyed by charged particle reactions there is no stellar production mechanism and the origin of these abundances is a long-standing problem. As discussed (e.g., by Prantzos 2007) irradiation by galactic cosmic rays (GCR) is a promising scenario but also associated with large uncertainties. Most likely a combination of the contributions from GCR irradiation and the  $\nu$  process in core-collapse supernovae is required to explain the solar abundance as pointed out by Prantzos (2012) and Austin et al. (2014).

To illustrate how the  $\nu$  process can produce the light elements the upper panel of Figure 3 shows the  $^7\text{Li}$  mass fraction as a function of the mass coordinate for a  $15 M_\odot$  progenitor model for the set of low neutrino energies as defined above. In order to disentangle the impact of electron type (anti)neutrinos and heavy flavor neutrinos results from calculations in which the neutrino reactions either only for charged-

**Table 1**

Production factors relative to solar abundances from [Lodders \(2003\)](#), normalized to  $^{16}\text{O}$  production. Shown are the results obtained without neutrino, with our choice of neutrino temperatures (“Low energies”), and with the choice of [Heger et al. \(2005\)](#) (“High energies”). For each set of energies, the results are also shown when only charged current reactions (induced by electron flavor neutrinos) are considered and when only neutral current reactions are considered.

Nucleus	no $\nu$	Low energies <sup>a</sup>			High energies <sup>b</sup>		
		with $\nu$	only charged current	only neutral current	with $\nu$	only charged current	only neutral current
$^7\text{Li}$	0.002	0.04	0.01	0.03	0.58	0.05	0.57
$^{11}\text{B}$	0.01	0.31	0.17	0.21	1.57	0.58	1.31
$^{15}\text{N}$	0.06	0.09	0.08	0.08	0.16	0.10	0.15
$^{19}\text{F}$	0.13	0.18	0.14	0.16	0.29	0.17	0.26
$^{138}\text{La}$	0.16	0.46	0.44	0.18	0.77	0.73	0.22
$^{180}\text{Ta}^c$	0.20	0.49	0.48	0.24	0.84	0.80	0.33

<sup>a</sup> $T_{\nu_e} = 2.8$  MeV,  $T_{\bar{\nu}_e} = T_{\nu_{\mu,\tau}} = 4.0$  MeV

<sup>b</sup> $T_{\nu_e} = 4.0$  MeV,  $T_{\bar{\nu}_e} = 5.0$  MeV,  $T_{\nu_{\mu,\tau}} = 6.0$  MeV

<sup>c</sup>Assuming that 35% survives in the long-lived isomeric state ([Mohr et al. 2007](#))

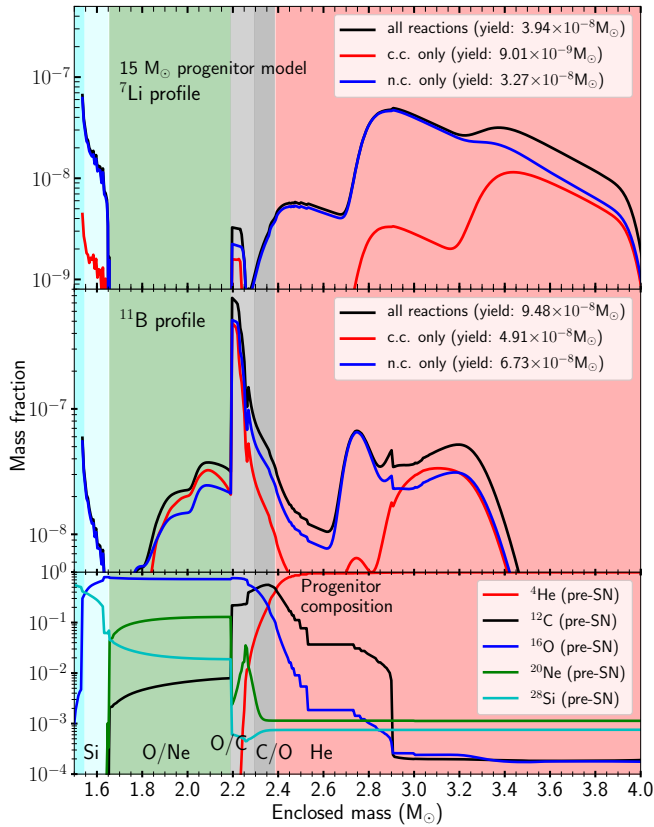


**Figure 3.** Profiles of  $^7\text{Li}$  and  $^{11}\text{B}$  mass fractions for the  $15 M_{\odot}$  using the updated low neutrino energies model with solar metallicity.  $^7\text{Li}$  is mostly made at the base of the He shell by the reaction sequence described in the text and  $^{11}\text{B}$  is produced in the thin C layer. Also shown are results when only charged current (c.c.) or only neutral current (n.c.) reactions are taken into account. This shows that electron flavor neutrinos contribute to as similar extent as the heavy flavor neutrinos for . The colored regions denote the different stellar regions as labeled in the bottom panel: Si shell (cyan), O shell (light cyan), O/Ne shell (green), O/C shell (grey), and He shell (red)

(c.c.) or only for neutral current (n.c.) process have been included are also shown.

At the base of the He-shell the neutral current neutrino-interactions  $^4\text{He}(\nu, \nu'p)$  and  $^4\text{He}(\nu, \nu'n)$  contribute to produce  $^7\text{Li}$  by the reactions  $^3\text{He}(\alpha, \gamma)^7\text{Be}(\beta^+)^7\text{Li}$  and  $^{11}\text{B}$  via  $^3\text{H}(\alpha, \gamma)^7\text{Li}(\alpha, \gamma)^{11}\text{B}$ . The same reaction chains operate on the  $\alpha$  rich freeze-out operating at the base of the Si shell in the most inner supernova ejecta near to the mass cut where the

material is subject to the most intense neutrino irradiation. This can be seen in [Figure 3](#) for the  $15 M_{\odot}$  progenitor model, where a noticeable mass fraction of  $^7\text{Li}$  and  $^{11}\text{B}$  are produced right at the edge of the mass cut. The contribution from this region to the total yield is of the order of a few percent and thus negligible in the models considered here, but it depends on the choice of the mass cut in parametric 1D simulations and is sensitive to details of the explosion dynamics. If the material is kept close to the neutron star for a longer time due to turbulent convection and is later ejected, the contribution of this region to the production of  $^7\text{Li}$  and  $^{11}\text{B}$  could be larger. A final answer to the role of the  $\nu$  process in this region therefore requires to take into account multi-D effects from self-consistent supernova simulations.

The bulk of  $^{11}\text{B}$  is produced in the thin C shell, see middle panel of [Figure 3](#), by neutral-current spallation reactions on  $^{12}\text{C}$ , i.e.,  $^{12}\text{C}(\nu, \nu'n/p)$ , that mostly produce  $^{11}\text{C}$  that decays later with a half-life of about 20 minutes to  $^{11}\text{B}$ . The charged current reactions  $^{12}\text{C}(\nu_e, e^-p)^{11}\text{C}$  and  $^{12}\text{C}(\bar{\nu}_e, e^+n)^{11}\text{B}$  contribute almost as much as the neutral current for the low energies. However, for the high energies the neutral current clearly dominates. This is also visible in the averaged values in [Table 1](#), where the production factors for the calculations with only neutral- and charged current reactions are also shown. It illustrates the increased importance of charged current processes for the “low energies” case. [Figure 3](#) also shows that there is a minor contribution to  $^{11}\text{B}$  in the O/Ne shell which is due to  $^{16}\text{O}(\nu, \nu'ap)$ . Such multi-particle emission channels have not been included in previous studies but are now taken into account for all nuclei in the reaction network.

The production of  $^7\text{Li}$  and  $^{11}\text{B}$  requires the knockout of protons and neutrons from tightly bound  $^4\text{He}$ ,  $^{12}\text{C}$  and  $^{16}\text{O}$  by high energy neutrinos from the tail of the distribution. Consequently, the shift of the neutrino spectra to lower energies has a significant impact on the production of these light elements. Due to the sensitivity of  $^7\text{Li}$  and  $^{11}\text{B}$  to the neutrino energies [Yoshida et al. \(2005\)](#) have suggested that the energies of  $\nu_{\mu,\tau}$  and  $\bar{\nu}_{\mu,\tau}$  can be constrained requiring a good reproduction of the solar abundance of  $^{11}\text{B}$  considering contributions from both cosmic-rays and  $\nu$  process. We use updated neutrino cross sections for reactions on  $^4\text{He}$  from [Gazit & Barnea \(2007\)](#) that are slightly larger than those previously used, giving an increase in the production of  $^7\text{Li}$  and  $^{11}\text{B}$  compared to the yields presented by [Heger et al. \(2005\)](#) when we use the same energies (“high energies” case). The same cross sections for  $^4\text{He}$  and also comparably low ener-

gies have also been used in a recent study by Banerjee et al. (2016) about the production of radioactive  $^{10}\text{Be}$  for a supernova model of a  $11.8 M_{\odot}$  progenitor.  $^{10}\text{Be}$  is mostly produced by the two proton emission channel  $^{12}\text{C}(\nu, \nu' pp)^{10}\text{Be}$  in the O/C shell and for the models studied here we obtain an average yield of  $3.9 \times 10^{-11} M_{\odot}$  for the low neutrino energies and  $2.5 \times 10^{-10} M_{\odot}$  for the high energies. Even with the high neutrino energies the  $\nu$  process does not produce enough  $^{10}\text{B}$  and  $^6\text{Li}$  to explain the solar system values. While the solar system value for  $^{11}\text{B}/^{10}\text{B}$  is around 4, the average value we get from our calculations is  $^{11}\text{B}/^{10}\text{B} \approx 100$ . Similarly we find  $^7\text{Li}/^6\text{Li} \approx 200$  compared to a solar system value of 12. Therefore, the abundances of  $^{10}\text{B}$  and  $^6\text{Li}$  require a contribution from cosmic ray spallation (e.g., Prantzos 2007) which also contributes to  $^{11}\text{B}$  and  $^7\text{Li}$ . Based on models for the production  $^{11}\text{B}$  and  $^{10}\text{B}$  by galactic cosmic rays (GCR), Austin et al. (2014) have estimated that the  $\nu$  process must produce about  $42 \pm 4\%$  of the solar  $^{11}\text{B}$  which is consistent with our estimate based on the “low energies” case.

We find that with realistic neutrino energies the production of  $^7\text{Li}$  by the  $\nu$  process is negligible. This is consistent with the observation of the Lithium “Spite plateau” (Spite & Spite 1982; Sbordone et al. 2010) in metal-poor stars in the metallicity range  $-3.0 \lesssim [\text{Fe}/\text{H}] \lesssim -1.5$ . The top panels of Figure 2 show that the neutrino enhanced yields of  $^7\text{Li}$  and  $^{11}\text{B}$  are not as sensitive to the progenitor model as, e.g.,  $^{19}\text{F}$ . This is because in the lower mass stars the relevant zones tend to be closer to the proto-neutron star which compensates for the overall narrower burning shells that contain smaller amounts of relevant seed nuclei. Since the production of  $^{16}\text{O}$  increases with progenitor mass that also means that the production factor normalized to  $^{16}\text{O}$  significantly increases towards the low mass end of the progenitor range we studied. Hence uncertainties in the initial mass function will also play an important role since the weight given to the low mass stars is crucial for the average production factor.

#### 4.2. $^{15}\text{N}$ , and $^{19}\text{F}$

The  $\nu$  process can contribute to the production of  $^{15}\text{N}$  and to  $^{19}\text{F}$  in the O/Ne and O/C shells mostly via the neutral current spallation of protons or neutrons  $^{16}\text{O}(\nu, \nu' p/n)$  and  $^{20}\text{Ne}(\nu, \nu' p/n)$  respectively, since  $^{15}\text{O}$  as well as  $^{19}\text{Ne}$  quickly decay to  $^{15}\text{N}$  and to  $^{19}\text{F}$  respectively. Even the charged current reactions  $^{16}\text{O}/^{20}\text{Ne}(\nu_e, e^- p)$  and  $^{16}\text{O}/^{20}\text{Ne}(\bar{\nu}_e, e^+ n)$  finally contribute to  $^{15}\text{N}$  and to  $^{19}\text{F}$ . When we take into account the harder spectrum for the heavy flavor neutrinos we find that the spectrally averaged cross section for the sum of the two charged current channels is a factor 10 smaller than the combined neutral current channels for the higher neutrino energies. For the lower energies the charged current contribution is now smaller by only a factor 3.

Heger et al. (2005) have already argued that this mechanism can probably not account for the entire solar abundance of  $^{19}\text{F}$  and can only produce small amounts of  $^{15}\text{N}$ . Table 1 shows that with the low neutrino energies the averaged  $^{19}\text{F}$  yield is increased by 30% but still only reaches a production factor of 0.2 and with high energies it is less than 0.3. This is in agreement with the conjecture that the  $\nu$  process in core-collapse supernovae is not the only source of  $^{19}\text{F}$  which is supported by recent observational evidence. Spectral analysis of nearby stars do not show a distinct correlation between O and F abundances that would be expected if supernovae were the

main source for Fluorine (Jönsson et al. 2017). Galactic chemical evolution models (Renda et al. 2004; Kobayashi et al. 2011), still attribute a significant component of the galactic  $^{19}\text{F}$  inventory to core collapse supernovae in combination with asymptotic giant branch (AGB) and Wolf-Rayet stars.

The lower panel of Figure 2 shows that the  $^{19}\text{F}$  yield exhibits a relatively large sensitivity to the progenitor model. Indeed, the mechanism behind the production depends significantly on the mass of the star.

For the  $15 M_{\odot}$  model the supernova shock alone, i.e., without neutrinos, increases the pre-supernova  $^{19}\text{F}$  content of  $4.3 \times 10^{-6} M_{\odot}$  to a yield of  $5.5 \times 10^{-6} M_{\odot}$ , corresponding to a production factor of 0.15. Neutrinos increase the production factor to 0.20 or 0.28 for low and high energies respectively. The thermonuclear component is mainly due to the reaction sequence  $^{18}\text{O}(p, \alpha)^{15}\text{N}(\alpha, \gamma)^{19}\text{F}$  operating on  $^{18}\text{O}$  at the lower edge of the He-shell where post shock temperatures reaches 0.67 GK at densities of up to  $1500 \text{ g cm}^{-3}$ . This requires an episode of convection to mix the  $^{18}\text{O}$  from the CNO cycle down to the bottom of the He-shell where the peak temperature in the shock will be optimal. For the least massive star, the  $13 M_{\odot}$  model  $^{18}\text{O}$  remains concentrated in a narrow region where the peak temperature reaches less than 0.5 GK and as a result the shock heating does not really play a role for the  $^{19}\text{F}$  yield without neutrinos which here results almost entirely from the pre-explosive hydrostatic burning and gives a production factor of 0.23. Including the  $\nu$  process in this model however gives the highest production factor among the models studied here of 0.27 for the low energies and 0.37 for high energies.

The profile of the  $^{19}\text{F}$  mass fraction for the  $15 M_{\odot}$  model is shown in the upper panel of Figure 4 where one can see that the thermonuclear production at the base of the He shell is confined to a relatively narrow region. The thermonuclear production of  $^{19}\text{F}$  requires two components. First the presence of  $^{18}\text{O}$  that is produced via  $^{14}\text{N}(\alpha, \gamma)^{18}\text{F}(\beta^+ \nu_e)^{18}\text{O}$ .  $^{14}\text{N}$  results from the CNO cycle and thus the region for suitable for the thermonuclear production of  $^{19}\text{F}$  is sensitive to the physics of Hydrogen burning. Secondly, the peak temperature reached in this region needs to be in the range of 0.4 – 0.5 GK.

Assuming that internal energy after shock passage is dominated by radiation one can relate the explosion energy  $E_{\text{expl}}$  and the peak temperature  $T_{\text{peak}}$  at a given radius  $r$  can as (Woosley et al. 2002):

$$T_{\text{peak}} = 2.4 \left( \frac{E_{\text{expl}}}{10^{51} \text{ erg}} \right)^{1/4} \left( \frac{r}{10^9 \text{ cm}} \right)^{-3/4} \text{ GK}. \quad (1)$$

This illustrates that whether the optimal temperature conditions for  $^{19}\text{F}$  production are reached for a given progenitor abundance profile is very sensitive to the radial position of the compositional shell interfaces and also mildly sensitive to the explosion energy. The optimal temperature itself is determined by thermonuclear reaction rates and recent updates on the proton capture rates (Iliadis et al. 2010) have a significant impact on the production of  $^{19}\text{F}$ . Compared to calculations with reaction rates based on Caughlan & Fowler (1988) and Angulo et al. (1999) the updated reaction rates have increased the total yield of  $^{19}\text{F}$  by 15% without neutrinos and by 20% with the high neutrino energies for the  $15 M_{\odot}$  model.

Trends of the  $^{19}\text{F}$  production with respect to the progenitor mass can be related to these sensitivities of the thermonuclear production. With increasing initial stellar mass the  $^{19}\text{F}$  pro-

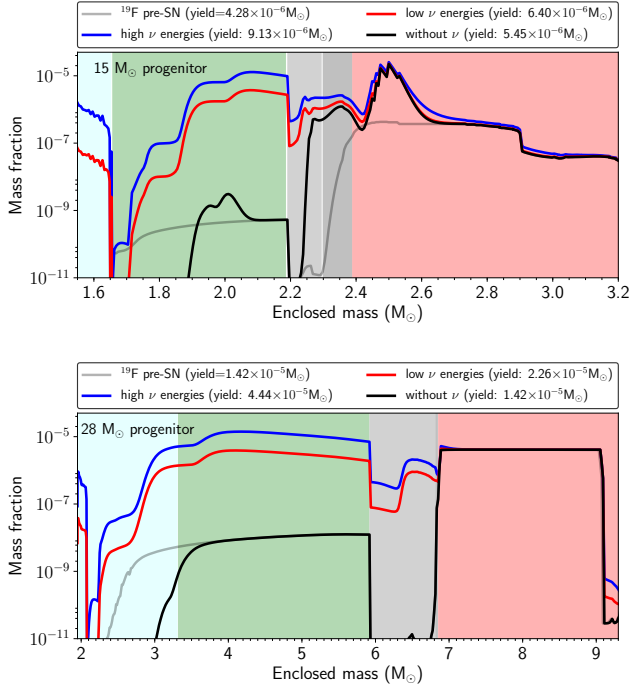


**Figure 4.** Mass fraction of  $^{19}\text{F}$  for the  $15 M_{\odot}$  model (upper panel) and the  $28 M_{\odot}$  progenitor (lower panel) representative for the lower and upper ends of the range of masses we explore. Shown are the pre-SN mass fractions as well as the final mass fractions without neutrinos, with the updated set of low neutrino energies and the high energies. While the supernova shock leads to a peak in the mass fraction around mass coordinate  $2.5 M_{\odot}$ , the  $\nu$  process is much more prominent for the more massive model. The background colors indicate the compositionally differing shells of the progenitor star as shown in detail at the bottom of Figure 3

duction factor without neutrinos tends to decrease because of a larger production of  $^{16}\text{O}$  even though the yield of  $^{19}\text{F}$  itself also increases substantially as can be seen in Figure 2. The  $\nu$  process has also a larger impact because the mass contained in the O/Ne layer increases while the thermonuclear production is increasingly suppressed. This is illustrated with two examples in Figure 4 where the mass fraction of  $^{19}\text{F}$  for the  $15 M_{\odot}$  and  $28 M_{\odot}$  models are shown, representative for lower and upper end of mass range considered here. For the  $28 M_{\odot}$  model the contribution from the  $\nu$  process in the O/Ne layer is the most prominent effect of the explosion while the peak of thermonuclear production at the inner He-shell in the  $15 M_{\odot}$  model gives an important contribution. For stars more massive than  $17 M_{\odot}$ , the  $\nu$  process can boost the  $^{19}\text{F}$  production by factors of up to 1.5-2 and 3-4 for low and high energies respectively.

In contrast to the sensitivity of the thermonuclear production mechanism to temperature and composition the  $\nu$  process is mainly sensitive to the distribution of  $^{20}\text{Ne}$  in the stellar model as well as the cross sections for neutrino induced reactions on  $^{20}\text{Ne}$ , which is now based on measured Gamow-Teller strength (Anderson et al. 1991; Heger et al. 2005). The remaining uncertainties in understanding the origin of  $^{19}\text{F}$  are therefore due to the stellar modeling and the thermonuclear reaction rates as well as the contribution from other astrophysical scenarios.

#### 4.3. Long-lived $^{138}\text{La}$ and nature's rarest element $^{180}\text{Ta}$

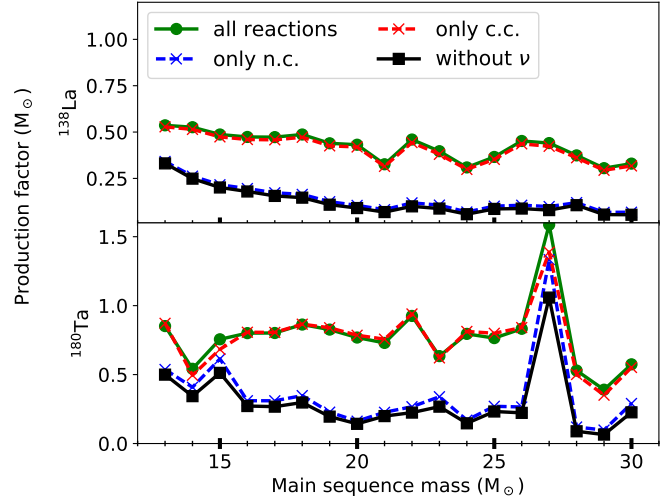


**Figure 5.** Production factors relative to  $^{16}\text{O}$  for  $^{138}\text{La}$  and  $^{180}\text{Ta}$  for the new set of low neutrino energies. Results including only neutral current (n.c.) and only charged current (c.c.) are also shown. Only for the  $14 M_{\odot}$ ,  $15 M_{\odot}$  and  $27 M_{\odot}$  models a significant contribution from neutral current reactions to the production of  $^{180}\text{Ta}$  appears while  $^{138}\text{La}$  is dominated by the c.c. reactions for all the models. The values for  $^{180}\text{Ta}$  correspond to the assumption that 35% of the yield survive in the long-lived isomeric state.

The production of the isotopes  $^{138}\text{La}$  and  $^{180}\text{Ta}$  is of particular interest because they both are present in the solar system but their production mechanism is not yet fully understood. In contrast to the nuclei discussed above which are strongly affected by neutral current reactions, the  $\nu$  process affects  $^{138}\text{La}$  and  $^{180}\text{Ta}$  almost exclusively via  $\nu_e$  captures. Therefore, those two isotopes are the most promising species to infer  $\nu_e$  properties via  $\nu$  process nucleosynthesis. The cross sections for  $^{138}\text{Ba}(\nu_e, e^-)^{138}\text{La}$  and  $^{180}\text{Hf}(\nu_e, e^-)^{180}\text{Ta}$  are well constrained based on experimentally measured transition strengths (Byelikov et al. 2007).

s-process nucleosynthesis calculations (Belic et al. 2002; Käppeler et al. 2004) have shown that around 80% of the solar  $^{180}\text{Ta}$  can be produced in AGB stars mostly via decays of excited states of  $^{179}\text{Hf}$  and  $^{180}\text{Hf}$ . However, Heger et al. (2005) have also found an overproduction of  $^{180}\text{Ta}$  due to the  $\nu$  process in core collapse supernovae.

Understanding the origin of  $^{180}\text{Ta}$  is further complicated by the fact that the  $J^{\pi} = 1^+$  ground state  $^{180}\text{Ta}$  decays by electron capture and  $\beta^-$  with a half-life of 8.15 h and only its isomeric  $9^-$  state at an excitation energy of 75 keV is very long lived. Due to its high spin, the isomeric state is effectively decoupled from the ground state at low temperatures. We do not treat  $^{180}\text{Ta}$  and its meta-stable isomeric state  $^{180}\text{Ta}^m$  as separate species in our network. A significant fraction of the  $^{180}\text{Ta}$  the ground state has already decayed at the end of our nucleosynthesis calculations at  $2.5 \times 10^4$  s. Therefore, we take the  $^{180}\text{Ta}$  abundance at 200 s after the start of the calculation when most of the produced  $^{180}\text{Ta}$  is still present and the thermal equilibrium between the ground state and the long-lived isomeric state has just frozen out. Following the estimates derived by Mohr et al. (2007) we assume that about 35% of  $^{180}\text{Ta}$  survives in the excited state.

Using the set of high neutrino energies, our results for  $^{138}\text{La}$  and  $^{180}\text{Ta}$  are consistent with those of presented by Heger et al. (2005) and Byelikov et al. (2007), giving almost solar production of  $^{138}\text{La}$  and  $^{180}\text{Ta}$ . The  $^{180}\text{Ta}$  production shown in table 1 and Figure 5 are corrected for the fact that only the isomeric

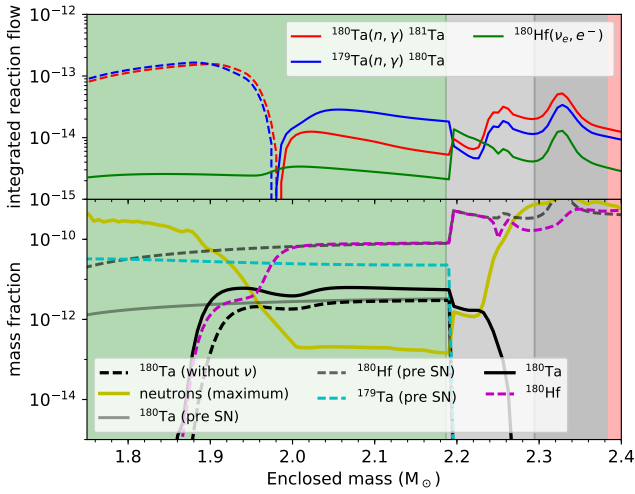


**Figure 6.** Time integrated reaction flows (top panel) and mass fraction profile of  $^{180}\text{Ta}$  and relevant nuclei (bottom panel) for the  $15 M_{\odot}$  model. If the forward  $(n, \gamma)$  is dominating flows are shown as solid lines while dashed lines indicate that the inverse process  $(\gamma, n)$  dominates. The neutrino induced reaction flow through  $^{180}\text{Hf}(\nu_e, e^-)^{180}\text{Ta}$  is also shown and only dominates in a very narrow region. The background colors indicate the different compositional layers as in Figure 3.

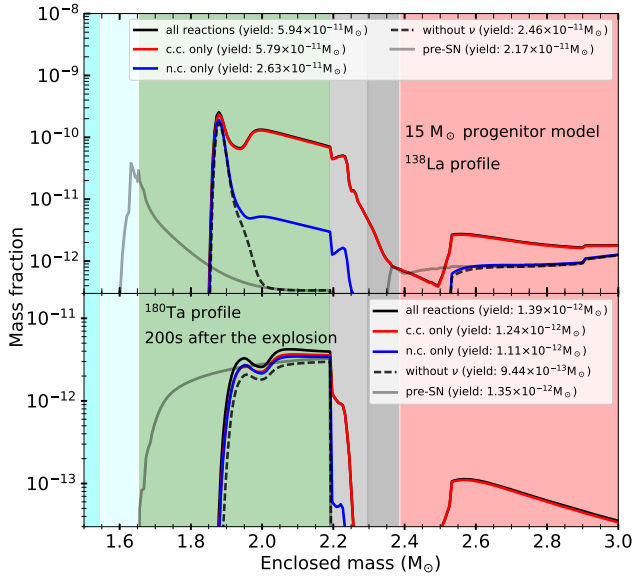


**Figure 7.** Mass fraction profiles of  $^{138}\text{La}$  and  $^{180}\text{Ta}$  for the  $15 M_{\odot}$  progenitor model. The background colors indicate the compositional zones as in 3. Also shown are results with only neutral and charged current reactions.  $^{138}\text{La}$  and  $^{180}\text{Ta}$  are both affected primarily by the charged current reactions with electron neutrinos.

state of  $^{180}\text{Ta}$  is long lived.

Figure 6 illustrates the production of  $^{180}\text{Ta}$  in the  $15 M_{\odot}$  model. The reaction flows have been estimated as integrated instantaneous flows based on the abundances at the beginning of each time step of the network calculation. At the base of the O/Ne shell, below  $1.9 M_{\odot}$  the peak temperature exceeds  $2.6 \text{ GK}$  and the density reaches  $5 \times 10^5 \text{ g cm}^{-3}$ . Under these conditions not only the pre-supernova abundance of  $^{180}\text{Ta}$  but also  $^{180}\text{Hf}$  are destroyed by photodissociation (see Figure 7). Since  $^{180}\text{Hf}$  is the target for the  $\nu_e$  captures, this marks the lower boundary of the production region. The prevalence of  $(\gamma, n)$  over  $(n, \gamma)$  is indicated by the dashed lines in the upper panel of Figure 6. Further out, as the peak temperature

decreases below  $2.3 \text{ GK}$ , the  $\gamma$  process leads to peak in the production of  $^{180}\text{Ta}$ . The  $\nu$  process increases the maximum abundance but only operates after the shock has passed and the material has cooled to below  $2 \text{ GK}$ .

For the particular case of the  $15 M_{\odot}$  model the pre SN abundance of  $^{179}\text{Ta}$  is larger than the  $^{180}\text{Ta}$  abundance. Therefore, not only the direct charged current channel  $^{180}\text{Hf}(\nu_e, e^-)^{180}\text{Ta}$  plays a role but also free neutrons mainly from  $^{16}\text{O}(\nu, \nu' n)$ ,  $^{24}\text{Mg}(\nu, \nu' n)$  and  $^{20}\text{Ne}(\nu, \nu' n)$  increase the final yield of  $^{180}\text{Ta}$ . Figure 7 shows that neutral current reactions alone lead to a significant increase of the final yield even though the contribution from  $^{180}\text{Hf}(\nu_e, e^-)^{180}\text{Ta}$  still dominates.

As the peak temperature is lower at a higher mass coordinate the conditions for an effective production via the  $\gamma$  process are no longer reached and the time integrated reaction flows change sign (see Figure 6). The competition between the  $^{179}\text{Ta}(n, \gamma)$  and  $^{180}\text{Ta}(n, \gamma)$  is important for the final abundance of  $^{180}\text{Ta}$  in this region. Wisshak et al. (2001) have presented measurements for the neutron capture cross section on  $^{180}\text{Ta}^m$  and we use the reaction rates from the KADoNiS v0.3 database (Dillmann et al. 2014) for both reactions.

At mass coordinate of  $2.0 M_{\odot}$  the main source for free neutrons changes from photodissociation to neutrino spallation. Without neutrinos, the initial  $^{180}\text{Ta}$  mass fraction remains unchanged in this region. Since this progenitor model provides a relatively high initial abundance of  $^{179}\text{Ta}$  both processes, the direct charged current and the neutral current providing additional free neutrons, are active.

Only in a small region between  $2.2$  and  $2.3 M_{\odot}$  do the  $\nu_e$  captures on  $^{180}\text{Hf}$  dominate the production. Further out in the He shell, free neutrons from  $^{22}\text{Ne}(\alpha, n)$  destroy any  $^{180}\text{Ta}$  that is produced by neutrinos, forming the upper boundary of the production region. The role of neutral current and charged current reactions depends significantly on the progenitor structure. In the range of progenitor models studied here the  $14$ ,  $15 M_{\odot}$  and  $27 M_{\odot}$  models are the only cases for which more than  $10\%$  of the  $\nu$  process contribution to  $^{180}\text{Ta}$  results from neutral current neutrino reactions due to the additional neutrons to be captured on  $^{179}\text{Ta}$  because those progenitor models are already enriched in  $^{179}\text{Ta}$  and  $^{180}\text{Ta}$  while at the same time depleted in  $^{180}\text{Hf}$ . The  $27 M_{\odot}$  stands out in particular because  $^{180}\text{Ta}$  is already produced to full solar abundance before the explosion and without neutrinos. The  $\nu$  process increases the production factor to  $1.5$  and  $2.5$  for low and high neutrino energies respectively. The pre-explosive production of  $^{179,180}\text{Ta}$  depends sensitively on the temperatures reached during the last burning stages. If the O/Ne shell becomes hot enough, photodissociation can change the abundances significantly. This shows that more detailed modeling of the pre supernova phase is desirable to understand not only the explosion mechanism as suggested by Suwa & Müller (2016) but it might also have a large effect on the synthesis of individual nuclear species.

As can be seen in Figure 5 the  $14$  and  $15 M_{\odot}$  stars also show a particularly low  $\nu$  process contribution to  $^{180}\text{Ta}$  and a relatively large  $^{180}\text{Ta}$  and low  $^{180}\text{Hf}$  abundance before the explosion, possibly as a result of slightly hotter burning conditions during the evolution. (This is also reflected in the  $^{98}\text{Tc}$  abundances shown in Figure 10.) The reaction cross section for  $^{180}\text{Hf}(\nu_e, e^-)^{179}\text{Ta}$  is comparable to  $^{180}\text{Hf}(\nu_e, e^-)^{180}\text{Ta}$  for average neutrino energies around  $10 \text{ MeV}$  such that  $^{179}\text{Ta}$  can also be produced in-situ. This process contributes  $10\text{-}20\%$  to the total  $^{180}\text{Ta}$  yield. Averaged over the whole range of



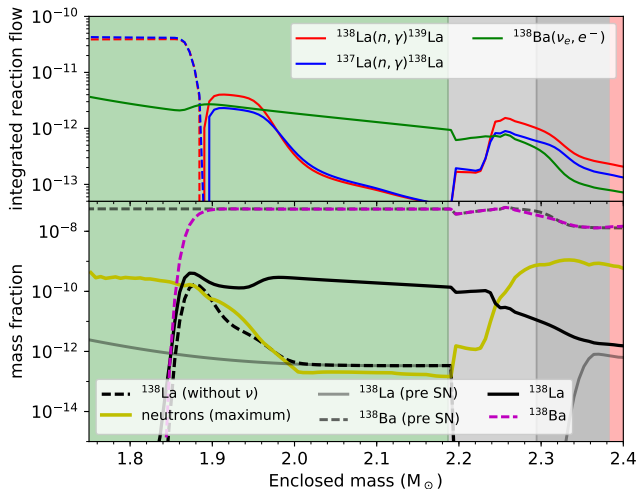


**Figure 8.** Same as Figure 6 but for  $^{138}\text{La}$ . There is also a peak in the production due to  $(\gamma, n)$  reactions and in this case there is a region between 2.0 and 2.3  $M_{\odot}$  where the  $\nu$  process clearly is the dominant production channel.

progenitors  $^{180}\text{Ta}$  is underproduced with the new set of lower neutrino energies (see table 1) ameliorating the tension with the contribution from the  $s$  process in AGB stars.

$^{138}\text{La}$  is also a  $p$  nucleus that is bypassed by the  $s$  process that moves along the chain of stable Barium isotopes. Figure 8 shows the most important reaction flows affecting  $^{138}\text{La}$ . Similar to the case of  $^{180}\text{Ta}$ , the production of  $^{138}\text{La}$  at the base of the O/Ne layer is dominated by the competition between  $(n, \gamma)$  and  $(\gamma, n)$  reactions, leading to a peak of the production even without neutrinos due to photodissociation of  $^{139}\text{La}$  at peak temperatures of around 2.4 GK. As the peak temperature drops below 2 GK neutron captures dominate and tend to move the material towards  $^{139}\text{La}$ . Without neutrinos, the supply of  $^{137}\text{La}$  is very small. However,  $^{138}\text{Ba}(\nu_e, e^-n)$  can lead to a substantial production of  $^{137}\text{La}$  because of the relatively large abundance of  $^{138}\text{Ba}$ . The cross section for the reaction  $^{138}\text{Ba}(\nu_e, e^-n)$  is based on the experimentally determined B(GT) strength [Byelikov et al. \(2007\)](#) in combination with branching ratios for particle emission from a statistical model as stated above.

In contrast to the case of  $^{180}\text{Ta}$  free neutrons from neutral current spallation reactions alone do not have a significant effect because the relevant target nucleus  $^{137}\text{La}$  is for all progenitors much less abundant than  $^{138}\text{Ba}$  and would need to be produced by the charged current reaction first. In our calculations about 10% of the total yield of  $^{138}\text{La}$  result from neutron captures on  $^{137}\text{La}$ . This contribution is sensitive to the ratio between the  $^{137}\text{La}(n, \gamma)$  and  $^{138}\text{La}(n, \gamma)$  cross sections. Therefore, we have taken the reaction rates by [Rauscher & Thielemann \(2000\)](#) in spite of recent experimental constraints on the  $^{138}\text{La}(n, \gamma)$  cross section ([Kheswa et al. 2015](#)).

In Figure 8 one can see that further out in the O/Ne shell where temperatures are too low to produce a significant neutron density by photodissociation the direct neutrino induced production is the dominating reaction flow, leading to an extended region where the  $^{138}\text{La}$  mass fraction is almost exclusively determined by  $\nu_e$ . Therefore, the production by the  $\nu$  process increases with the amount of mass in the O/Ne shell.

The upper panel of Figure 5 shows the production factor for  $^{138}\text{La}$  over the range of progenitor models discussed here with the set of our set of low neutrino energies. Figure 5 also shows the results of calculations with only neutral current and

charged current reactions, illustrating that the charged current channel clearly dominates over the whole range of progenitors. The most striking feature is an overly large production of  $^{138}\text{La}$  for the 28  $M_{\odot}$  model. This is due to an increased production of Ba isotopes during the pre-supernova evolution. This progenitor is also enhanced in weak  $s$  process nuclei. More massive progenitors contain more mass in the O/Ne layer and correspondingly give larger yields of  $^{138}\text{La}$  and  $^{180}\text{Ta}$ . When looking at the production factors this increase of the yield is compensated by an also increasing yield of  $^{16}\text{O}$  and the decreasing weight of more massive stars in the IMF.

$^{138}\text{La}$  and  $^{180}\text{Ta}$  are mostly sensitive to electron flavor neutrinos and since the production region in the O/Ne shell is closer to the proto-neutron star they are also the most sensitive to neutrino emission properties. Therefore, those nuclei might also be affected the most by collective neutrino oscillations as suggested by [Wu et al. \(2015\)](#).

#### 4.4. Further effects on stable isotopes

Recent studies dedicated to the  $\nu$  process have focused on individual nuclei and have employed limited sets of neutrino-nucleus cross-sections expected to be relevant for the nuclei of interest. In particular when such approaches focus on a single progenitor model, the question whether there are additional effects in other scenarios or due to different reactions that have not been included always remains open. With our complete set of cross sections we can survey the whole range of the reaction network at once and study for the first time the complete effect of  $\nu$ -reactions on the explosive nucleosynthesis in supernovae for a whole range of progenitor models. The abundances of stable nuclei in the solar system are one of our most accurately measured observables making processes that have an effect on those nuclei particularly important. Unless major changes in the models for the progenitor composition or the supernova mechanism itself are found, we hope to have captured all possible processes and give in the following a summary of the changes of the yields of stable nuclei after decay, before we enter on the discussion of radioactive isotopes in §5.

Table 2 summarizes the maximum differences  $\delta_{rel} = (Y_{no\nu} - Y_{\nu})/Y_{no\nu}$  in the integrated yields of stable and very long-lived ( $T_{1/2} > 10^{10}$  years) nuclei after decay that we find among all the progenitor models studied here. The table shows that large effects that change abundances by a significant factor indeed only appear for nuclei that have been identified in previous studies. On the 10% level we find a few more nuclei that are affected. In most cases the maximum effect is found for the more massive progenitors. That is because the inner regions of more massive stars tend to be more compact, putting the relevant O/Ne layer closer to the PNS. Only the light isotopes  $^7\text{Li}$  and  $^9\text{Be}$  that are produced at larger radii in the He-shell are maximally affected in at the low mass end of our progenitor range because here the He-shell is at smaller radii. Even though  $^9\text{Be}$  and  $^{10}\text{B}$  are listed in Table 2 their yields correspond to production factors of at most  $4.5 \times 10^{-2}$  and  $7 \times 10^{-2}$  respectively, too low to explain their solar abundances or solar ratios with respect to  $^7\text{Li}$  and  $^{11}\text{B}$ . However, models of GCR nucleosynthesis can account for those nuclei as stated in §4.1. A modification of  $^{17}\text{O}$  mass fraction is found throughout the O/Ne shell and is mostly induced by neutron captures on abundant  $^{16}\text{O}$  where the neutrons are released by neutral-current spallation reactions. Locally the mass fraction of  $^{17}\text{O}$  is increased by several orders of magnitude. However, the to-

tal yield is dominated by the abundance of  $^{17}\text{O}$  in the He-shell left over from H-burning via the CNO cycle. The modification of  $^{33}\text{S}$  occurs in the Si/O shell and it is affected by several reactions, including the reaction sequence  $^{34}\text{S}(\nu_e, e^-)^{34}\text{Cl}(\gamma, p)$  as well as  $^{34}\text{S}(\nu, \nu'n)^{33}\text{S}$ . Thus, the contributions of charged- and neutral-current reactions is about equal. At the top of the O/Si shell  $^{35}\text{Cl}$  is enhanced by  $^{36}\text{Ar}(\nu, \nu'p)$  where  $^{36}\text{Ar}$  is a results of the  $\alpha$ -rich freeze out. The production factor for  $^{35}\text{Cl}$  on average around 0.5, making the contribution from massive stars a relevant for the solar system inventory of  $^{35}\text{Cl}$ . The yield of  $^{41}\text{K}$  is modified mostly by  $^{41}\text{Ca}(\bar{\nu}_e, e^+)$  and to a lesser extent by  $^{42}\text{Ca}(\nu, \nu'p)$ . Averaged over the range of progenitors the  $\nu$  process increases the production factor for  $^{41}\text{K}$  from 0.48 to 0.52 for the low neutrino energies but it reaches values of up to 1.8 for the 20  $M_\odot$  progenitor for which the effect of neutrinos is negligible.  $^{176}\text{Lu}$  is affected by electron antineutrino capture on  $^{176}\text{Hf}$  which is inherited from the initial metallicity in the O/Ne shell, very similar to the cases of  $^{138}\text{La}$  and  $^{180}\text{Ta}$  but interestingly involving antineutrinos in this case. The IMF averaged production factor is however below 0.2.  $^{176}\text{Lu}$  can be explained with the main  $s$ -process in AGB-stars and subject of current experimental efforts (Roig et al. 2016). The case of  $^{176}\text{Lu}$  is further complicated by a short-lived  $1^-$  excited state at 122 keV above the  $7^-$  ground state that  $\beta$  decays with a half-life of 3.7 h. The short lived isomer is likely to be populated thermally under supernova conditions and since we do not include it explicitly in our calculations we expect that our results overestimate the yield of  $^{176}\text{Lu}$ . In contrast to that  $^{113}\text{In}$  is a p-nucleus that is also produced via the  $\gamma$ -process. Neutrinos affect its yield by  $\nu_e$  captures on  $^{113}\text{Cd}$  in the O/Ne shell where the mass fraction is increased by up to a factor of 500 to values of up to  $3 \times 10^{-12}$  which is still a factor ten smaller than the abundance inherited from the initial metallicity. This isotope is particularly interesting because Travaglio et al. (2011) found it to be underproduced in type Ia supernovae. However, in our calculation we also find a production factor of at most 0.32 because the abundance in the O/Ne shell is still low compared to the solar abundance. The optical model potentials to describe the involved  $(\gamma, \alpha)$  reactions have recently been studied by Kiss et al. (2013) where a good agreement of the total cross-sections with the theoretical calculations was found. We find that the final integrated yield of  $^{59}\text{Co}$  is reduced by 11% in the 15  $M_\odot$  model. This is due to  $^{59}\text{Ni}(\nu_e, e^-)^{58}\text{Cu}$  which reduces the abundance of the long-lived  $^{59}\text{Ni}$  with a half-life of  $7.6 \times 10^4$  yr that finally decays to  $^{59}\text{Co}$ . The modification of the  $^{57}\text{Fe}$  results mostly from the charged-current reaction  $^{58}\text{Ni}(\bar{\nu}_e, e^+p)$  and also involves  $^{58}\text{Co}(\nu, \nu'p)$ . The 12% increase in the yield of  $^{54}\text{Cr}$  for the 23  $M_\odot$  reflects the production of  $^{54}\text{Mn}$  by  $\bar{\nu}_e$  capture on  $^{54}\text{Fe}$  that reaches a mass fraction of  $5 \times 10^{-2}$  the O/Si shell. We see that in the O/Si shell close to the mass cut reactions on the Fe-peak elements induce some changes on the ejecta composition on the order of few percent. However, since our piston model is not expected to give a very good description of these innermost regions (Young & Fryer 2007) that are sensitive to the imposed mass cut and potential fallback of material, further studies with self-consistent explosion models are needed to verify the significance of these effects. Heger et al. (2005) have suggested reactions that could modify the yields of  $^{51}\text{V}$ ,  $^{55}\text{Mn}$ ,  $^{78}\text{Kr}$ ,  $^{138}\text{Ce}$  and  $^{196}\text{Hg}$ . Our calculations include all the reactions suggested by Heger et al. (2005) and we find that the yields of these nuclei are increased by 5-9%. The effects on

the  $p$ -nuclei  $^{113}\text{In}$ ,  $^{137}\text{La}$  and  $^{180}\text{Ta}$  shown here also illustrate that it is necessary to include neutrino-induced reactions for quantitative predictions of  $\gamma$ -process nucleosynthesis.

**Table 2**

Maximum values of the relative difference  $\delta_{rel}^{max} = (Y_\nu - Y_{no\nu})/Y_{no\nu}$  that are larger than 10% from all progenitor models considered here for the set of low neutrino energies. Also shown are the yields in  $M_\odot$  for the calculations with and without including neutrino reactions. The last column gives the mass of the progenitor for which the maximum value is found  $M_*^{max}$ .

Nucleus	$\delta_{rel}^{max}(\%)$	$Y_{no\nu}(M_\odot)$	$Y_\nu(M_\odot)$	$M_*^{max}(M_\odot)$
$^7\text{Li}$	2, 250	$1.69 \times 10^{-9}$	$3.96 \times 10^{-8}$	15
$^9\text{Be}$	25	$7.19 \times 10^{-11}$	$8.97 \times 10^{-11}$	18
$^{10}\text{B}$	34	$1.79 \times 10^{-9}$	$2.40 \times 10^{-9}$	25
$^{11}\text{B}$	8, 208	$5.78 \times 10^{-9}$	$4.80 \times 10^{-7}$	25
$^{15}\text{N}$	188	$2.58 \times 10^{-5}$	$7.45 \times 10^{-5}$	30
$^{17}\text{O}$	16	$5.98 \times 10^{-5}$	$6.91 \times 10^{-5}$	30
$^{19}\text{F}$	88	$6.92 \times 10^{-6}$	$1.30 \times 10^{-5}$	20
$^{33}\text{S}$	14	$3.75 \times 10^{-4}$	$4.26 \times 10^{-4}$	19
$^{35}\text{Cl}$	11	$3.91 \times 10^{-4}$	$4.35 \times 10^{-4}$	25
$^{41}\text{K}$	22	$2.82 \times 10^{-5}$	$3.44 \times 10^{-5}$	19
$^{54}\text{Cr}$	12	$3.07 \times 10^{-5}$	$3.43 \times 10^{-5}$	23
$^{57}\text{Fe}$	13	$4.66 \times 10^{-3}$	$5.25 \times 10^{-3}$	25
$^{59}\text{Co}$	-12	$8.42 \times 10^{-4}$	$7.39 \times 10^{-4}$	17
$^{78}\text{Kr}$	10	$3.63 \times 10^{-8}$	$3.26 \times 10^{-8}$	23
$^{113}\text{In}$	19	$5.44 \times 10^{-10}$	$6.48 \times 10^{-10}$	27
$^{138}\text{La}$	511	$5.35 \times 10^{-11}$	$3.27 \times 10^{-10}$	30
$^{176}\text{Lu}$	14	$1.79 \times 10^{-10}$	$2.04 \times 10^{-10}$	30
$^{180}\text{Ta}$	501	$4.93 \times 10^{-13}$	$2.96 \times 10^{-12}$	29

Unless significant changes in the progenitor composition or the neutrino properties are found, we can thus exclude and further effects on stable nuclei due to the  $\nu$  process on supernova nucleosynthesis for stars in the mass range 13-30  $M_\odot$  at solar metallicity.

## 5. RADIOACTIVE NUCLEI

### 5.1. Overview

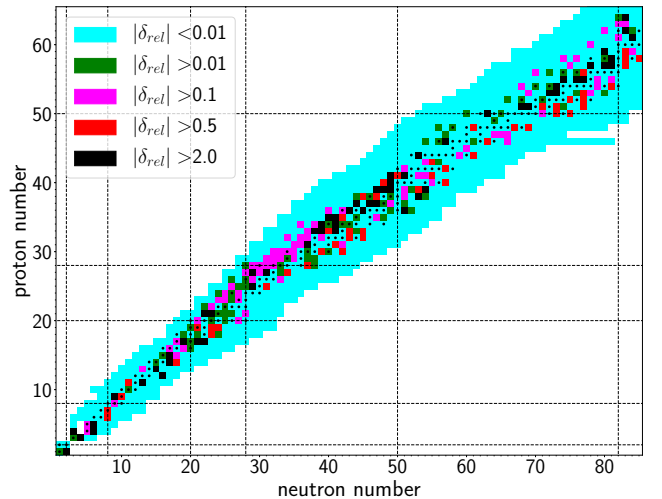


**Figure 9.** Maximum values among all the progenitors studied here for the absolute of the relative change  $\delta_{rel}$  as defined in Figure 12 with the new set of low neutrino energies at  $2.5 \times 10^4$  s after core bounce when the very short lived nuclei have already decayed. Only nuclei with a mass fraction larger than  $10^{-12}$  are included.

In addition to the important effect on the yields of stable isotopes we will see in the following that the  $\nu$  process affects the production of many radioactive nuclei. Mostly, the modification of the abundances of radioactive nuclei does not result in noticeable changes of the yields of stable nuclei after the radioactive isotopes have decayed. However, for some species the decay is accompanied by the emission of characteristic  $\gamma$ -rays and others leave traces in the composition of pre-solar grains. The most interesting cases are discussed in detail in §5.2 and §5.3 but before we give an overview of the effects on radioactive nuclei, focusing on the 15  $M_{\odot}$  progenitor model as a representative example for the mass range we have explored.

We find that a large range of radioactive species are substantially affected by the  $\nu$  process. Figure 9 provides an overview of the relative effects of the  $\nu$  process for the whole range of nuclei included in our calculations at 7 hours after the explosion when very short lived nuclei have already decayed. The relative differences  $\delta_{rel}$  shown there, are the maximum values we find for the whole range of progenitor models we have looked at. The largest effects appear close to stability where seed nuclei with a large abundances relative to their neighbors are present. Many nuclei are affected on the 10% level and a few show differences exceeding 50% or a factor 2. Below the Iron group the  $\nu$  process mostly increases the production of isolated rare stable and long-lived nuclei discussed in the previous sections. Spallation reactions on the most abundant nuclei like  $^{16}\text{O}$ ,  $^{20}\text{Ne}$  and  $^{24}\text{Mg}$  do not change the abundances of the targets noticeably but the neighboring nuclei get produced and they provide light particles that affect other nuclei. Additional neutrons are mostly captured by heavier nuclei, leading to increased abundances on the neutron rich side for  $A > 100$  where the seed nuclei are inherited from the initial solar metallicity. Since the  $\gamma$  process also operates on those seed nuclei, the abundances on the proton-rich side are also modified slightly. Around the Iron group many long-lived nuclei exist and they are mainly produced in the Si-shell close to the PNS where the neutrino fluxes are largest. After freeze out from NSE, neutrino interactions reshuffle the abundances of the Fe-peak with differences at the 10% level, leading for example to the modification of the  $^{59}\text{Co}$  yields discussed previously. In the region of  $A = 60 - 90$  we can see a significant modification of the abundances, both on the neutron- and proton-rich side of stability. This is due to the weak  $s$ -process nuclei and the operation of the  $\gamma$ -process that already leads to the production of radioactive nuclei in that region which are then modified further by neutrino interactions. Radioactive, neutron-deficient isotopes of As, Br, Kr, Sr, Y and Zr are particularly enhanced with mass fraction typically between  $10^{-12}$  to  $10^{-10}$ . For progenitors with a weaker  $\gamma$  process free neutrons from spallation reactions are captured on the most abundant  $s$ -process nuclei and lead to increased abundances on the neutron-rich side in the same mass region.

The production of radioisotopes by the  $\nu$  process has hitherto received only limited attention in the literature which has mostly focused on the five isotopes discussed above. In the following we will discuss the overall effect of the  $\nu$  process on the production of radioactive nuclei, in particular focusing on those that are relevant for observations.

Table 3 lists the IMF averaged nucleosynthesis yields for a range of radioactive nuclei that are still present at around 7h after the explosion, including  $^{32}\text{P}$ ,  $^{72}\text{As}$ ,  $^{84}\text{Rb}$ ,  $^{88}\text{Y}$ . Their yields are increased by factors between 2 and 10 with the re-

Table 3

Impact of the  $\nu$  process on the yields of radioactive isotopes at the end of our calculation at  $2.5 \times 10^4$  s. At this time the very short-lived nuclei have already decayed and mostly species that are potentially interesting for observations remain. Shown are the yields in units of  $M_{\odot}$  averaged with an IMF as above, obtained without neutrino, with our choice of neutrino temperatures (“Low energies”), and with the choice of Heger et al. (2005) (“High energies”).

Nucleus	$T_{1/2}$	no $\nu$	Low energies <sup>a</sup>	High energies <sup>b</sup>
$^{22}\text{Na}$	2.61 yr	$1.89 \times 10^{-6}$	$2.42 \times 10^{-6}$	$3.01 \times 10^{-6}$
$^{26}\text{Al}$	0.72 Myr	$3.88 \times 10^{-5}$	$4.19 \times 10^{-5}$	$4.74 \times 10^{-5}$
$^{36}\text{Cl}$	0.30 Myr	$2.89 \times 10^{-6}$	$4.19 \times 10^{-6}$	$5.01 \times 10^{-6}$
$^{44}\text{Ti}$	59.1 yr	$3.68 \times 10^{-5}$	$5.05 \times 10^{-5}$	$5.17 \times 10^{-5}$
$^{60}\text{Fe}$	2.6 Myr	$7.20 \times 10^{-5}$	$7.21 \times 10^{-5}$	$7.23 \times 10^{-5}$
$^{72}\text{As}$	26.0 h	$2.38 \times 10^{-10}$	$3.01 \times 10^{-9}$	$7.48 \times 10^{-9}$
$^{84}\text{Rb}$	32.8 d	$3.97 \times 10^{-10}$	$2.87 \times 10^{-9}$	$5.50 \times 10^{-9}$
$^{88}\text{Y}$	106.6 d	$4.14 \times 10^{-10}$	$1.27 \times 10^{-9}$	$2.49 \times 10^{-9}$
$^{92}\text{Nb}$	34.7 Myr	$3.30 \times 10^{-11}$	$7.38 \times 10^{-11}$	$1.30 \times 10^{-10}$
$^{98}\text{Tc}$	4.2 Myr	$2.57 \times 10^{-11}$	$2.98 \times 10^{-11}$	$3.61 \times 10^{-11}$

$$^a T_{\nu_e} = 2.8 \text{ MeV}, T_{\bar{\nu}_e} = T_{\nu_{\mu,\tau}} = 4.0 \text{ MeV}$$

$$^b T_{\nu_e} = 4.0 \text{ MeV}, T_{\bar{\nu}_e} = 5.0 \text{ MeV}, T_{\nu_{\mu,\tau}} = 6.0 \text{ MeV}$$

alistic neutrino energies and the production of  $^{72}\text{As}$  would be increased by almost two orders of magnitude with the choice of high neutrino energies. The typical yields for  $^{72}\text{As}$ ,  $^{84}\text{Rb}$ , and  $^{88}\text{Y}$  are  $10^{-9} M_{\odot}$ , which may allow for the observation of the gamma-ray decay lines only with very high precision observations. Further complicating the detection, their lifetimes are of the order of a 100 days or shorter, putting their decay signal in competition with  $^{56}\text{Ni}$  and its daughter  $^{56}\text{Co}$  which by far dominates the early lightcurve and therefore outshines the signature of the  $\nu$  process. However, this shows that the  $\nu$  process can affect a large range of radioactive nuclei among which we can look for a suitable candidate to provide an observable signature of supernova neutrinos.

### 5.2. Short-lived radionuclides $^{36}\text{Cl}$ , $^{92}\text{Nb}$ and $^{98}\text{Tc}$ in the late input scenario

Isotopic ratios mostly derived from mass spectroscopy of grains of meteoritic material have proven to be an invaluable source of information on stellar nucleosynthesis (Zinner 1998; McKeegan & Davis 2003; Dauphas & Chaussidon 2011). While  $^{138}\text{La}$  and  $^{180}\text{Ta}$  are measurable as part of the current composition of the solar system, indications for the presence of now extinct radioactive nuclei, such as  $^{36}\text{Cl}$  and  $^{92}\text{Nb}$  have been found in (Schönbächler et al. 2002; Lin et al. 2005; Jacobsen et al. 2009) primitive meteorites that are assumed to have conserved the composition of the material from which the solar system has formed. For  $^{98}\text{Tc}$  a positive detection is still missing, but upper limits are given by Dauphas et al. (2002) and Becker & Walker (2003). In the following we discuss the production of  $^{92}\text{Nb}$ ,  $^{98}\text{Tc}$  and  $^{36}\text{Cl}$  in detail and compare the observed abundance ratios from primitive meteorites.

Our calculations show (see Table 3), that neutrino interactions increase the average yield of  $^{36}\text{Cl}$  by factors of 1.76 and 2.1 for low and high neutrino energies respectively and  $^{92}\text{Nb}$  by a factors of 2.1 and 3.7. This relatively large increase that does not vary a lot with the neutrino energies indicates that the  $\nu$  process provides a dominant and independent contribution. Even though the total yield of  $^{98}\text{Tc}$  is increased by less than 20% locally the mass fraction of  $^{98}\text{Tc}$  in the O/Ne shell is typically increased by one to two orders of magnitude be-

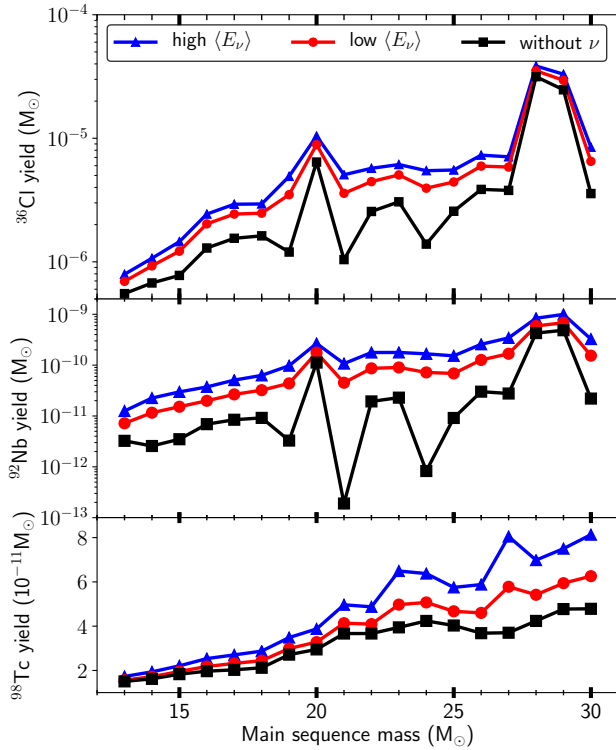


**Figure 10.** Yields of  $^{36}\text{Cl}$ ,  $^{92}\text{Nb}$  and  $^{98}\text{Tc}$  for different sets of neutrino energies and without the  $\nu$  process over the range of progenitors considered here. Note that the upper two panels are on a logarithmic scale while the  $^{98}\text{Tc}$  mass fraction is on a linear scale because it shows a much smaller variation.

cause the total yield is dominated by the pre-supernova content of  $^{98}\text{Tc}$  in the He-shell. The enhancement is mostly due to  $^{98}\text{Mo}(\nu_e, e^-)$ . Despite the higher average energy of electron antineutrinos  $^{98}\text{Ru}(\bar{\nu}_e, e^+)$  is negligible because  $^{98}\text{Ru}$  is very rare with mass fractions typically around  $10^{-16}$ , while  $^{98}\text{Mo}$  is much more abundant with mass fractions around  $5 \times 10^{-9}$ . A particularly large amount of  $^{98}\text{Mo}$  is present in the  $27 M_\odot$  which is enriched in  $\gamma$  process nuclei as discussed for the case  $^{180}\text{Ta}$  in §4.3. For most progenitor models there is also a direct contribution of the  $\gamma$  process during the shock heating to  $^{98}\text{Tc}$  which is less than 10% of the  $\nu$  process contribution.

Figure 10 shows the yields of  $^{36}\text{Cl}$ ,  $^{92}\text{Nb}$  and  $^{98}\text{Tc}$  for the stellar models we have studied.  $^{36}\text{Cl}$  and  $^{92}\text{Nb}$  exhibit very similar systematics with respect to the progenitor mass because they are both very sensitive to the composition and temperature at the inner edge of the O/Ne shell.  $^{36}\text{Cl}$  and  $^{92}\text{Nb}$  are the two species with the deepest  $\nu$  process production region. While their yields including the  $\nu$  process are relatively smooth with respect to the initial progenitor mass, large variations can be seen in the calculations without neutrinos. As a result, also the relative enhancement ranges from factors of 2-5 for most progenitors up to a factor of 600 for the  $24 M_\odot$  model which yields particularly little  $^{92}\text{Nb}$  without the  $\nu$  process. The production mechanisms for  $^{92}\text{Nb}$  and  $^{98}\text{Tc}$  in the  $\nu$  process are very similar to the production of  $^{138}\text{La}$  and  $^{180}\text{Ta}$ . The upper panel of Figure 11 shows the dominating reaction flows relevant for the synthesis of  $^{92}\text{Nb}$  in the  $15 M_\odot$  progenitor model. At the bottom of the O/Ne shell, photodissociation and neutron captures compete and in an optimal temperature

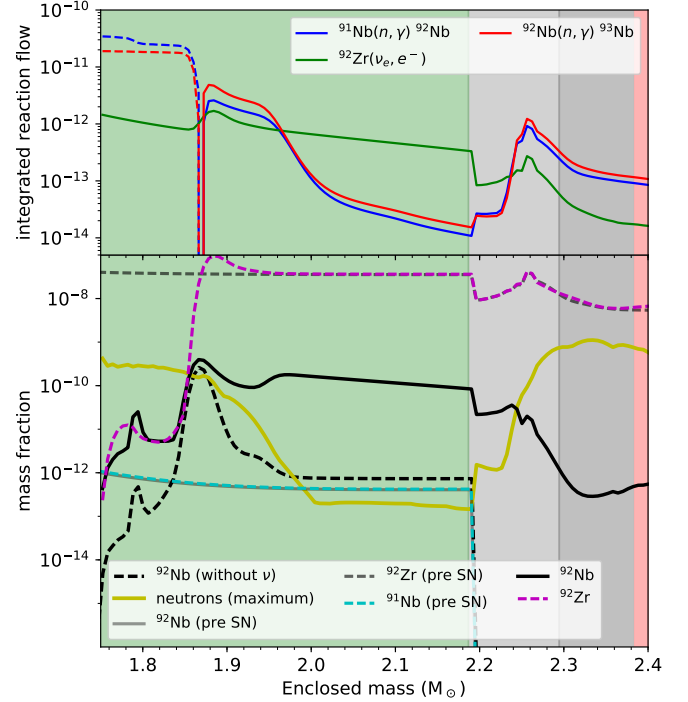


**Figure 11.** Same as Figure 8 for  $^{92}\text{Nb}$ . The top panel shows time integrated reaction flows and the lower panel gives an overview over the mass fractions of the involved nuclei. While the production of  $^{92}\text{Nb}$  proceeds via  $(n, \gamma)$ - $(\gamma, n)$  reactions in the deeper, hotter part of the O/Ne shell, the  $\nu$  process leads to a moderate production throughout the outer part of the O/Ne shell.

range the  $^{92}\text{Nb}$  mass fraction forms a peak even without neutrinos. The  $\nu$  process contributes evenly through the whole region which contains  $^{92}\text{Zr}$  with a mass fraction of around  $3 \times 10^{-8}$ .

The  $^{36}\text{Cl}$  yield without neutrinos results mostly from neutron captures on  $^{35}\text{Cl}$  at lower to mid O/Ne shell.  $^{35}\text{Cl}$  is present in the progenitor but is also produced by the shock heating. Providing additional neutrons, neutrino neutral current spallation reactions have a minor effect on the yield while  $^{36}\text{Ar}(\bar{\nu}_e, e^-)^{36}\text{Cl}$  is the most important contribution of the  $\nu$  process for all of the progenitor models. During O-burning  $^{36}\text{Ar}$  is copiously produced reaching mass fractions of the order  $10^{-2}$  in the final Si-shell. This  $^{36}\text{Ar}$ -rich is exposed to temperatures exceeding 3 GK and does not contribute to the  $\nu$  process. In the  $15 M_\odot$  model  $^{36}\text{Ar}$  is efficiently produced by  $^{35}\text{Cl}(p, \gamma)$  and  $^{32}\text{S}(\alpha, \gamma)$  at the bottom of the O/Ne shell where the peak temperature reaches up to 2.5 GK. While for most other nuclei that are affected by the  $\nu$  process, the parent nucleus is already present in the progenitor,  $^{36}\text{Ar}$  and also  $^{35}\text{Cl}$  first need to be produced by the shock heating. Hence,  $^{36}\text{Cl}$  is also particularly sensitive to the shock propagation and the explosion energy.

For the progenitors more massive than  $15 M_\odot$  the production region moves to smaller radii, into the upper part of the Si-shell which also contains substantial amounts of Oxygen. The  $20 M_\odot$  model stands out with a rather large pre-supernova production. In this model the  $\nu$  process contribution is strongest in the Si/O-O/Ne transition region which consists of Si and Ne in roughly equal amounts.

Cheoun et al. (2012) and Hayakawa et al. (2013) have discussed the  $\nu$  process in supernovae as a production site for the radioactive isotopes  $^{92}\text{Nb}$  and  $^{98}\text{Tc}$ . In particular  $^{92}\text{Nb}$  is inter-

esting as a potential chronometer. [Mohr \(2016\)](#) has analyzed the impact of an isomeric state of  $^{92}\text{Nb}$  at 135.5 keV on its nucleosynthesis in an explosive environment and found that it does not affect the production. The survival might however be affected by a reduced lifetime at low temperatures. The yields of  $^{92}\text{Nb}$  and  $^{98}\text{Tc}$  might even be more enhanced by contributions from the neutrino-driven wind ([Fuller & Meyer 1995](#); [Hoffman et al. 1996](#)) which we do not include here.

Due to their long lifetimes and very low abundance  $^{92}\text{Nb}$  and  $^{98}\text{Tc}$  are not suited for  $\gamma$  ray astronomy and  $^{36}\text{Cl}$  decays mainly to the ground-state of  $^{36}\text{Ar}$  without characteristic  $\gamma$ -rays. Therefore, we need other observational constraints if we want to use the production of these nuclides to learn about supernova neutrinos. Evidence for the presence of  $^{92}\text{Nb}$  ([Schönbächler et al. 2002](#)) and  $^{36}\text{Cl}$  ([Jacobsen et al. 2009](#)) at the time the solar system has formed have been found in meteoritic grains (see also [Wasserburg et al. \(2006\)](#) for an overview).

[Hayakawa et al. \(2013\)](#) have estimated the contribution of the  $\nu$  process to the ISM inventory of  $^{92}\text{Nb}/^{93}\text{Nb}$  based on 11  $M_{\odot}$  supernova model. They conclude that the continuous uniform production is insufficient to explain the isotopic ratio of  $\approx 10^{-5}$  inferred from primitive meteorites ([Schönbächler et al. 2002](#)). While the estimate by [Hayakawa et al. \(2013\)](#) is based on a single progenitor model we can use the IMF weighted average of the stellar models we have studies. We get an average ratio of  $\langle^{92}\text{Nb}/^{93}\text{Nb}\rangle = 7.2 \times 10^{-4}$  without neutrinos. This reaches  $1.5 \times 10^{-3}$  and  $2.6 \times 10^{-3}$  for low and high neutrino energies respectively. Assuming a uniform production model and taking supernovae as the sole production site for both  $^{92}\text{Nb}$  and  $^{93}\text{Nb}$  we estimate the ratio as ([Huss et al. 2009](#)):

$$\left(\frac{X(^{92}\text{Nb})}{X(^{93}\text{Nb})}\right)_{UP} \approx 2 \langle^{92}\text{Nb}/^{93}\text{Nb}\rangle \frac{\tau_{92\text{Nb}}}{T} \quad (2)$$

Where  $\tau_{92\text{Nb}} = 50.1$  Myr is the decay timescale of  $^{92}\text{Nb}$ . With a typical isolation time  $T = 10$  Gyr we get a maximum ratio of  $1.3 \times 10^{-7}$  in agreement with [Hayakawa et al. \(2013\)](#) and still insufficient to explain the observed ratio. [Hayakawa et al. \(2013\)](#) conclude that a late injection event where the pre-solar material is polluted by the ejecta from a nearby supernova is more likely. [Banerjee et al. \(2016\)](#) have recently consolidated this scenario using the short-lived radioactive  $^{10}\text{Be}$  produced by the  $\nu$  process in low-mass supernovae as indicator. In the case of such a late input scenario, we can relate the measured abundance ratios to a single nucleosynthesis event. If this is the case, properties of this event can be inferred from measured abundance ratios. The main parameters are the delay time  $\Delta$  between the injection event and the condensation of the material into solids and the dilution factor  $f$  that indicates to which extent the solar system material has been mixed with the ejecta from the last event. Following [Takigawa et al. \(2008\)](#) and [Banerjee et al. \(2016\)](#) we can estimate the number ratio  $N_R/N_S$  between a radioactive isotope with mass number  $A_R$  and a stable reference nucleus with mass  $A_S$  at solar system formation as

$$\left(\frac{N_R}{N_S}\right)_{SSF} \approx \frac{f \times Y_R e^{-\Delta/\tau}}{X_S^{\odot} M_{\odot}} \times \frac{A_R}{A_S}. \quad (3)$$

where  $\Delta$  is the time between the last nucleosynthesis event to produce the isotope of interest and the condensation of the material into solid grains.  $Y_R$  is the yield of the radioactive nucleus in solar masses from our calculations and  $X_S^{\odot}$  is the

solar mass fraction of the reference isotope, taken here from [Lodders \(2003\)](#). Due to its long half-life,  $^{92}\text{Nb}$  is not very sensitive to  $\Delta$  and therefore a good candidate to constrain  $f$ . Assuming  $\Delta \approx 1$  Myr and the lowest  $^{92}\text{Nb}$  yield from the 13  $M_{\odot}$  model we require a dilution factor  $f \approx 5 \times 10^{-3}$  to achieve the measured ratio of  $1.6 \times 10^{-5}$  ([Schönbächler et al. 2002](#)). This value is significantly higher than what has been suggested in the literature ([Banerjee et al. 2016](#); [Takigawa et al. 2008](#); [Wasserburg et al. 2006](#)). Furthermore, this value is also much larger than the upper limit of  $f < 5 \times 10^{-4}$  that results from with the same model from the upper limit on the  $^{98}\text{Tc}/^{96}\text{Ru}$  ratio ([Becker & Walker 2003](#)). Thus, in particular with the updated neutrino energies, it does not seem possible to explain the pre-solar abundance of  $^{92}\text{Nb}$  with the input by a low mass supernova.

[Jacobsen et al. \(2009\)](#) have given a value of  $(17.2 \pm 2.5) \times 10^{-6}$  for the ratio  $^{36}\text{Cl}/^{35}\text{Cl}$  from grains of the Allende meteorite and [Lin et al. \(2005\)](#) have found a value of  $5 \times 10^{-6}$  in material from the Ningqiang carbonaceous chondrite, giving a combined range of possible values of roughly  $(3 - 20) \times 10^{-6}$ . [Jacobsen et al. \(2011\)](#) have suggested that late-stage irradiation of the proto-planetary disk is the most likely origin of pre-solar  $^{36}\text{Cl}$  while a stellar origin cannot be excluded. Using again our 13  $M_{\odot}$  model with  $\Delta = 1$  Myr and  $f = 5 \times 10^{-4}$  as suggested by [Banerjee et al. \(2016\)](#) we find  $^{36}\text{Cl}/^{35}\text{Cl}$  ratios of  $(8.3 - 9.5) \times 10^{-6}$  for low and high neutrino energies respectively compared to a ratio of  $6 \times 10^{-6}$  for the yields without neutrinos. All of these values are currently consistent with the range of observed ratios. However, the scaling of the  $^{36}\text{Cl}/^{35}\text{Cl}$  ratio with the neutrino energies make this nucleus an interesting candidate as neutrino thermometer if the parameters of the late input scenario and the meteoritic ratio can be determined with better precision in the future.

### 5.3. $\gamma$ -ray sources $^{22}\text{Na}$ and $^{26}\text{Al}$

The characteristic  $\gamma$ -ray lines of the decay of long lived  $^{26}\text{Al}$  has allowed ([Diehl 2013](#)) to estimate its present-day equilibrium content in the Galaxy to be  $2.8 \pm 0.8 M_{\odot}$ . While the sensitivity of  $^{26}\text{Al}$  yields from massive stars with respect to thermonuclear reaction rates has been studied in detail by [Iliadis et al. \(2011\)](#), we here explore the uncertainties related to the  $\nu$  process.

The yield of  $^{26}\text{Al}$  is known to be enhanced by neutrino nucleosynthesis ([Woosley et al. 1990](#); [Timmes et al. 1995](#)). We also find that the yield of  $^{26}\text{Al}$  is increased by factors between 1.1 and 1.4 in the range of progenitor models studied (see [Table 3](#) and [Figure 12](#)). For low energies the maximum increase is limited to a factor of 1.13 for the most massive progenitor in our set. For the high neutrino energies, the enhancement is within the precision of the galactic  $^{26}\text{Al}$  content estimate.

In massive stars  $^{26}\text{Al}$  can be produced in core H burning, C burning in the core, and in a convective shell as well as during explosive Ne/C burning in the supernova shock.  $^{26}\text{Al}$  from H core burning survives largely in the envelope and is partly blown away by stellar winds especially for more massive stars. It contributes 25%–55% of the total yield with the exception of the 13  $M_{\odot}$  progenitor for which the H burning component constitutes 70%. This component is unaffected by the explosion and by the neutrinos.

[Figure 13](#) shows the  $^{26}\text{Al}$  mass fraction profile for the 15  $M_{\odot}$  model which contains a significant amount of  $^{26}\text{Al}$  from C-burning in the O/Ne shell before the supernova ex-

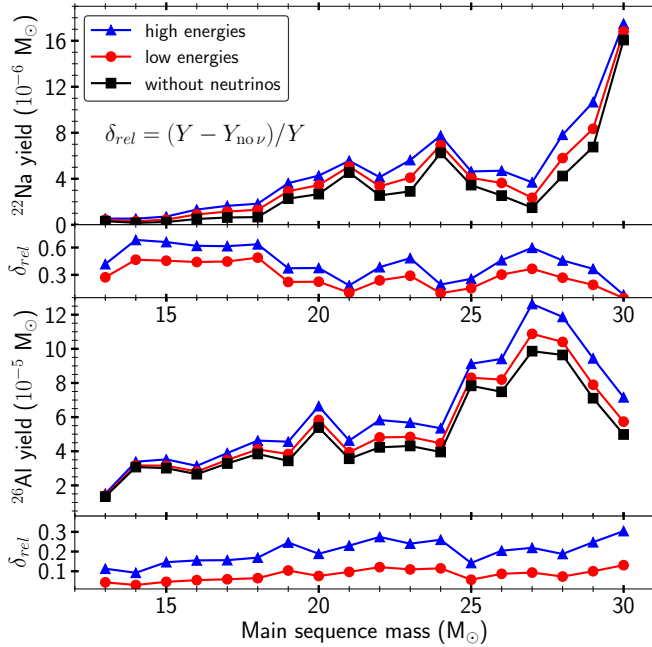


**Figure 12.** Yields of  $^{22}\text{Na}$  (upper panel) and  $^{26}\text{Al}$  (lower panel) for the set of progenitor stars considered here. Shown are the yields without neutrinos and including neutrinos with the high energies and the more realistic low energies. Below each panel the relative differences  $\delta_{rel} = (Y - Y_{\text{no}\nu})/Y$  between the yields with and without neutrinos are shown in smaller panels.

plosion. Most of this  $^{26}\text{Al}$  is destroyed by the shock, mainly by  $^{26}\text{Al}(n, p)^{26}\text{Mg}$  and  $^{26}\text{Al}(n, \alpha)^{23}\text{Na}$ . The  $19 M_{\odot}$  model shown in the right panel of Figure 13 differs significantly in its pre-supernova  $^{26}\text{Al}$  mass fraction which is almost negligible. However, both cases lead to a rather similar distribution and yield of  $^{26}\text{Al}$  at the end. When looking at the whole range of progenitors we find that the final  $^{26}\text{Al}$  yield in the ejecta is effectively independent of the inner C-burning component of pre supernova  $^{26}\text{Al}$ . Similar results have been obtained by Limongi & Chieffi (2006) for a different set of progenitor models.

Shock heating produces a peak in the mass fraction distribution during explosive C/Ne burning. The reactions chain  $^{20}\text{Ne}(\alpha, \gamma)^{24}\text{Mg}(n, \gamma)^{25}\text{Mg}(p, \gamma)^{26}\text{Al}$  competes with neutron induced reactions on  $^{26}\text{Al}$  and photodissociation at higher temperatures. The optimal conditions for the production of  $^{26}\text{Al}$  are found where the peak temperature reaches around 2.3–2.5 GK, depending on the progenitors density structure. With the explosion model used here we find for all progenitors a peak in the O/Ne shell. Deeper inside, i.e., left of the peak, no  $^{26}\text{Al}$  survives the shock heating while the  $\nu$  process can operate further out.

Neutrinos contribute to the production of  $^{26}\text{Al}$  during the explosive phase by two different mechanisms. Neutrino-induced spallation reactions on the most abundant nuclei in the O/Ne shell,  $^{20}\text{Ne}$ ,  $^{24}\text{Mg}$ , and  $^{16}\text{O}$  increase the number of free protons, enhancing the reaction  $^{25}\text{Mg}(p, \gamma)$ , which is also the main production channel without neutrinos. Additionally, the charged-current reaction  $^{26}\text{Mg}(\nu_e, e^-)$  also contributes with a cross section that is now based on experimental data as described in §2. Figure 13 illustrates the neutral-current and charged-current contributions. With the softer neutrino spectra, we find that both charged- and neutral-current reactions contribute to a similar extent to the production of  $^{26}\text{Al}$  in

the O/Ne layer. The enhancement of the  $^{25}\text{Mg}(p, \gamma)$  is confined to a narrow region of optimal temperature, whereas the  $^{26}\text{Mg}(\nu_e, e^-)$  contributes more evenly but to a lesser extent throughout the entire layer, decreasing with the neutrino flux at larger radii. The strength of the  $\nu$  process also depends on the position of the  $^{26}\text{Al}$  production peak within the O/Ne shell which in turn depends on the peak temperature. The deeper inside the peak is, the more mass is on the right hand side of the peak where the  $\nu$  process can operate efficiently. While the total mass of the O/Ne layer scales with the initial progenitor mass, the condition of the peak temperature is more sensitive to the detailed structure of the individual stellar models. Comparing the two cases in Figure 13 also illustrates this dependence of the  $\nu$  process region on the position of the  $^{26}\text{Al}$  peak. The systematics of the total yield with respect to the progenitor mass that are shown in Figure 12 follow the trend of the  $^{20}\text{Ne}$  content of the pre-supernova models, modulated by structural details affecting the position of the  $^{26}\text{Al}$  peak within the O/Ne layer.

The relative differences  $\delta_{rel}$  due to neutrinos to Figure 12 can be understood from these aspects. For the 13–18  $M_{\odot}$  progenitors, the  $^{26}\text{Al}$  peak is located in the middle of the O/Ne shell, such that only a fraction of that shell is cold enough for the  $\nu$  process to contribute. Within this range of progenitors the mass in the O/Ne shell increases giving rise to a slight increase with progenitor mass. In all of these models a substantial amount of  $^{26}\text{Al}$  is present from hydrostatic burning but little of it survives the high temperatures during the explosion. Starting from the 19  $M_{\odot}$  the  $^{26}\text{Al}$  peak is right at the bottom edge of the O/Ne shell. As discussed by Woosley et al. (2002) energy generation in central C burning in stars heavier than this can no longer overcome the neutrino losses which leads to substantial changes in structure and nucleosynthesis, including a reduced abundance of  $^{26}\text{Al}$  in the O/Ne shell. In the mass range between 19–25  $M_{\odot}$  there is basically no contribution from C burning and the  $\nu$  process has the strongest relative effect on  $^{26}\text{Al}$  because most of the O/Ne shell is cold enough. The 20  $M_{\odot}$  is a particular exception for which a convective merger of shells has occurred and altered the structure and composition (see also Woosley et al. 2002). The relatively large yields for the 25–28  $M_{\odot}$  progenitor models result from a drastic increase of the contribution from hydrostatic C burning that decreases again in the 29 and 30  $M_{\odot}$  progenitors. The 25–28  $M_{\odot}$  progenitors also exhibit the largest compactness parameter (O’Connor & Ott 2011)

$$\xi_{2.5} = \frac{2.5M_{\odot}}{R(M_r = 2.5M_{\odot})/1000\text{km}} \quad (4)$$

in the range between 0.31–0.45 and also the largest pre-SN content of  $^{25}\text{Mg}$ . Note that according the explosion criterion suggested by Ugliano et al. (2012), stars with  $\xi_{2.5} > 0.35$  are likely to fail to explode as supernovae.

The fact that the  $\nu$  process mostly adds to  $^{26}\text{Al}$  in a secondary way, i.e., by enhancing the abundance of protons, makes its contribution to scale smoothly with the  $\nu$  energy compared to the weak dependence with the neutrino energy seen in §4.3 and §5.2.

Since the position of the  $^{26}\text{Al}$  production peak depends on the peak temperature at that radius we can see from equation 1 that it also depends on the explosion energy. For less energetic explosions the optimal temperature is reached for smaller radii and a stronger impact of  $\nu$  process can be ex-

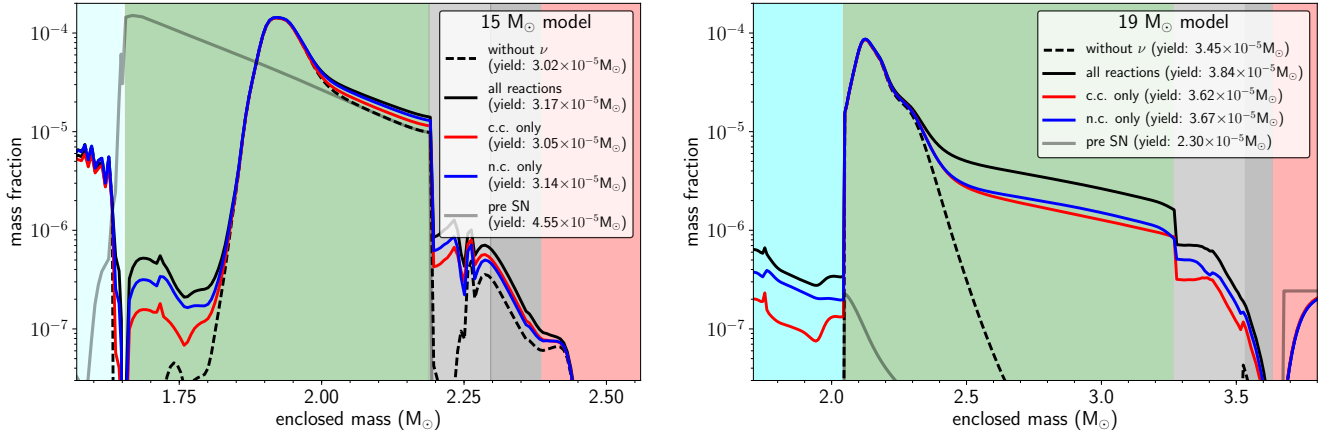


**Figure 13.** Mass fraction of  $^{26}\text{Al}$  for the  $15 M_{\odot}$  (left) and  $19 M_{\odot}$  (right) progenitor models. Shown are the results for calculations with and without including neutrino interactions, with charged-current reactions only, and neutral-current reactions only for the low neutrino energies. The pre-supernova mass fraction are also shown. Comparison of the two models illustrates that the contribution from hydrostatic C-burning almost irrelevant for the final yield.

pected because the neutrino fluxes are higher closer to the PNS.

The short-lived isomeric state of  $^{26}\text{Al}$  is not treated explicitly in our calculation, but we assume a thermal equilibrium and use an accordingly adjusted  $\beta$ -decay rate (Fuller et al. 1982). The validity of this assumption in a supernova environment has been confirmed by Iliadis et al. (2011).

Our results show that the major uncertainty for the yields of  $^{26}\text{Al}$  from massive stars originates from thermonuclear reaction rates. Iliadis et al. (2011) have estimated such a uncertainty to be a factor 3. As experiment and theory advance, these uncertainties are bound to shrink and the predictions can approach the precision of the observations.

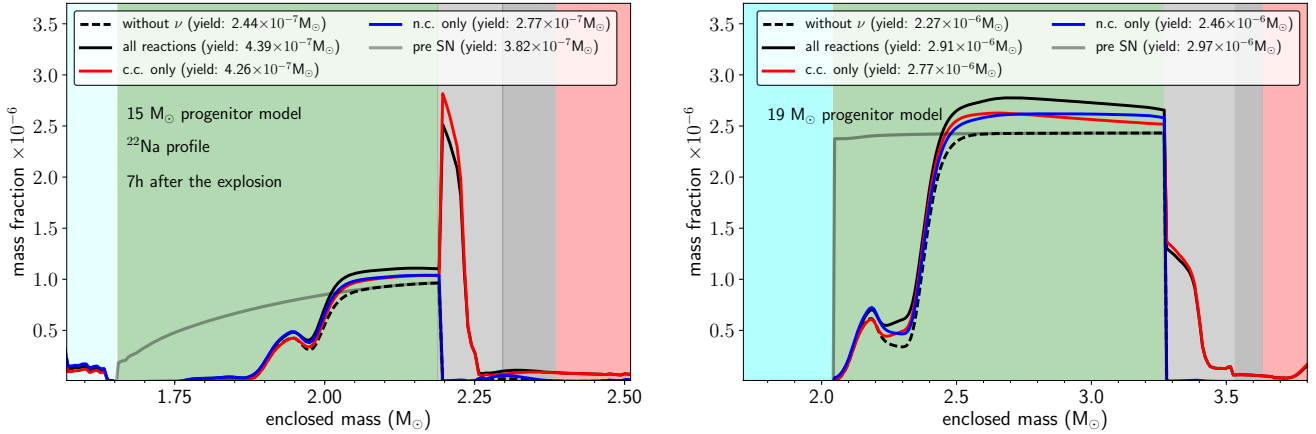
The radioisotope  $^{22}\text{Na}$  has a relatively short half-life of 2.6 yr and decays to  $^{22}\text{Ne}$  emitting a positron followed by the emission of a  $\gamma$  ray line at 1.275 MeV and two 0.511 MeV  $\gamma$  rays from the annihilation of the positron. Woosley et al. (1989) have estimated the contribution of  $^{22}\text{Na}$  to the bolometric lightcurve and emission lines from SN1987A based on a model that did not include the  $\nu$  process. They conclude that a detection of the  $\gamma$ -ray line emission might become possible with future instruments. In the following we describe how the  $\nu$  process affects the production of  $^{22}\text{Na}$  for our range of progenitor models and discuss the detectability of this enhancement in photometry and as radiogenic  $^{22}\text{Ne}$  in pre-solar grains.

Figure 12 shows that supernovae could eject even larger amounts of  $^{22}\text{Na}$  but representing a much smaller fraction of the total mass of the ejecta. The last phases of shell burning produce mass fractions around  $1\text{--}4 \times 10^{-6}$  of  $^{22}\text{Na}$  O/Ne shell. Without taking into account the  $\nu$  process the final ejected amount of  $^{22}\text{Na}$  is only determined by how much of it survives the shock heating which destroys  $^{22}\text{Na}$  for temperatures above 1.8 GK. Just like in the case of  $^{26}\text{Al}$  the peak temperatures reached in the O/Ne shell are the determining factor for the ejected amount of  $^{22}\text{Na}$ . In general, there is no contribution from pre-supernova wind and from the He shell or H envelope because most of the  $^{22}\text{Na}$  that has been produced there during hydrostatic burning has decayed at the time of core collapse. Figure 14 illustrates the distribution of the mass fraction of  $^{22}\text{Na}$  for the 15 and  $19 M_{\odot}$  progenitor models. At mass coordinates around  $1.9 M_{\odot}$  for the  $15 M_{\odot}$  model and around  $2.1 M_{\odot}$  for the  $19 M_{\odot}$  model there is also a small peak

in the mass fraction that results mostly from  $^{21}\text{Ne}(p, \gamma)^{22}\text{Na}$  competing with the neutron captures.

The  $\nu$  process affects this feature by changing the abundance of free protons as in the case of  $^{26}\text{Al}$  discussed above. This peak is however always negligible compared to the bulk of the  $^{22}\text{Na}$  in the outer part of the O/Ne shell which remains mostly unchanged by the passage of the supernova shock without taking into account neutrinos. The  $\nu$  process liberates free protons that increase of the  $^{22}\text{Na}$  mass fraction in the outer O/Ne shell as can be seen in Figure 14 and also the charged current reaction  $^{22}\text{Ne}(\nu_e, e^-)^{22}\text{Na}$  contributes.  $^{23}\text{Na}(\nu, \nu' n)^{22}\text{Na}$  has been suggested by Woosley et al. (1990) as an additional source of  $^{22}\text{Na}$ . We find that this channel contributes 50% of the neutral current effects for the  $16 M_{\odot}$  model. Figure 14 illustrates that both channels contribute to about the same extend in the outer O/Ne shell. This can be understood from the pre-supernova composition because the O/Ne shell consists of roughly equal mass fractions of  $^{22}\text{Ne}$  and  $^{21}\text{Ne}$  that range between  $5 \times 10^{-5}$  to  $5 \times 10^{-4}$  in the O/Ne shell of this progenitor.

More striking is the effect of the charged current  $^{22}\text{Ne}(\nu_e, e^-)^{22}\text{Na}$  reaction that increases the mass fraction of  $^{22}\text{Na}$  in the O/C shell and produced the very prominent peak for the  $15 M_{\odot}$  progenitor that can be seen in the left panel of Figure 14. In contrast, this production channel is negligible in the  $19 M_{\odot}$  model shown in the right panel. The O/C shell contains very little  $^{21}\text{Ne}$  and therefore thermonuclear and also neutral current contributions to  $^{22}\text{Na}$  are suppressed. The mass fraction of  $^{22}\text{Ne}$  in the O/C shell which has not undergone C-burning is between  $1\text{--}1.5 \times 10^{-2}$  and very similar for all progenitor models studied here. Still, only the  $14\text{--}18 M_{\odot}$  models show a major production of  $^{22}\text{Na}$  in the O/C shell due to the  $\nu_e$  capture on  $^{22}\text{Ne}$  that contributes at least 80% of the total  $\nu$  process enhancement for the progenitors in that range. That is reflected in larger values for  $\delta_{rel}$  in Figure 12. As described above, the energy balance of C burning changes and consequently also the star's structure, when going from the 18 to the  $19 M_{\odot}$  model. While the inner edge of the O/C shell is located between 17,000 and 20,000 km for progenitor models below  $19 M_{\odot}$ , its position moves out to more than 30,000 km for most of the more massive models. This reduces the maximum neutrino flux by more than a factor two and the neutrino induced production is suppressed. The abundance of  $^{22}\text{Na}$  in



**Figure 14.**  $^{22}\text{Na}$  mass fraction profile for the 15 (left) and 19  $M_{\odot}$  (right) progenitors for the set of low neutrino energies. While O/C shell contains the largest amount of  $^{22}\text{Na}$  the 15  $M_{\odot}$  model the contribution from this region is negligible for the 15  $M_{\odot}$  progenitor.

the outer part of the O/Ne shell is then much larger than at the bottom of the O/C shell for the more massive models. The 27  $M_{\odot}$  model is again an exception for which the abundances in both regions are similar again. That is because the 27  $M_{\odot}$  model has very little  $^4\text{He}$  left in the O/C shell, such that the neutron production via  $^{22}\text{Ne}(\alpha, n)$ , which drives the destruction of  $^{22}\text{Na}$  by neutron captures, is suppressed. For all the cases studied here, the  $^{22}\text{Na}$  yield with only charged current reactions is larger than with only neutral current reactions. For the low neutrino energies the charged current alone contributes at least 70% of the total  $\nu$  process enhancement and for the higher energies it is at least 60%.

Assuming a total yield of  $2 \times 10^{-6} M_{\odot}$  of  $^{22}\text{Na}$  Woosley et al. (1990) found that the contribution of the  $^{22}\text{Na}$  decay to the supernova lightcurve is of the order of  $10^{36}$  erg/s, very similar to the contribution from  $^{44}\text{Ti}$  decay during the first 2-3 years. During this time, the decay of  $^{56}\text{Co}$  still dominates the bolometric luminosity with  $10^{40}$ - $10^{38}$  erg/s. Later  $^{44}\text{Ti}$  with a half-life of 59 years dominates the luminosity while most of the  $^{22}\text{Na}$  has already decayed. Therefore, we do not expect the enhancement of  $^{22}\text{Na}$  due to the  $\nu$  process to make a difference for the bolometric lightcurve of a supernova (see also Kozma & Fransson (1998) and Diehl & Timmes (1998)). The  $\gamma$ -ray line at 1.275 MeV has been detected with the COMPTEL experiment on board the Compton Gamma-Ray Observatory associated with Nova Cassiopeia 1995. From this observation Iyudin (2010) has estimated the total amount of ejected  $^{22}\text{Na}$  to be  $\approx 10^{-7} M_{\odot}$  with large uncertainties remaining due to the distance ( $\approx 3\text{kpc}$ ) and total ejected mass ( $\approx 10^{-3} M_{\odot}$ ). Scaling the results from Woosley et al. (1989) for a supernova at a distance of 10 kpc with an escape fraction of 20% at 400 days after the explosion we find a photon flux of  $5.3 \times 10^{-6} \text{cm}^{-2}\text{s}^{-1}$  per  $10^{-6} M_{\odot}$  of ejected  $^{22}\text{Na}$ . Teegarden & Watanabe (2006) give the sensitivity of the SPI  $\gamma$ -ray telescope on the INTEGRAL satellite as  $1.2 \times 10^{-4}$  for the 1.275 MeV  $\gamma$ -ray line. The expected photon flux for the largest amount of  $^{22}\text{Na}$  we find for the 30  $M_{\odot}$  model would barely lead to such a photon flux. In order to distinguish between the low and high energy scenario discussed here, we would require to resolve a flux difference of  $5 \times 10^{-6} \text{photons cm}^{-2}\text{s}^{-1}$  which might become feasible with future space based  $\gamma$ -ray telescopes like the proposed e-ASTROGAM mission (Tatischeff et al. 2016).

In addition to the emission in the electromagnetic spectrum

$^{22}\text{Na}$  might also be relevant as the progenitor of  $^{22}\text{Ne}$  found in meteoritic grains. Clayton (1975) has already pointed out that the  $^{22}\text{Ne}$ -rich Ne-E(L) component in low density graphite grains from meteorites first found by Black & Pepin (1969) could be a consequence of  $^{22}\text{Na}$  decay, i.e., the Ne found in these grains would be pure  $^{22}\text{Ne}$  originally condensed as  $^{22}\text{Na}$ . More recently Amari (2009) has concluded that the O/Ne shell of massive stars are the most likely origin of the material with very low  $^{20}\text{Ne}/^{22}\text{Ne}$  ratios below 0.01. The condensation of graphite grains in O-rich material is problematic (Lattimer et al. 1978) even though models exist that would allow for it (Clayton et al. 1999). The C/O ratio in the O/Ne shell is typically  $\text{C/O} \approx 0.01$  while this ratio reaches  $\text{C/O} \approx 0.3$  in the O/C shell where charged current reactions produce most of the  $^{22}\text{Na}$ . Modest mixing with the C/O shell right on top of it could easily lead to material satisfying  $\text{C/O} > 1$  and strongly enriched in  $^{22}\text{Na}$ . The  $\nu$  process allows for the production of a large fraction of  $^{22}\text{Na}$  in more C-rich supernova ejecta but the ratio of  $^{12}\text{C}/^{13}\text{C} \approx 10^4$ - $10^5$  in these layers still requires mixing with the outer He or H rich layers to explain the high  $^{12}\text{C}/^{13}\text{C}$  ratio of  $313 \pm 2$  found in the same grains (Meier et al. 2012).

$^{44}\text{Ti}$  has been detected in supernova remnants (Iyudin et al. 1994; Grefenstette et al. 2014). It is produced mainly in the inner ejecta in an  $\alpha$ -rich freeze out of NSE Woosley et al. (2002). At high temperatures, photon- and charged particle induced reactions dominate over any neutrino contribution. Therefore, we find no significant effect of neutrinos on the yield of  $^{44}\text{Ti}$ . The production of  $^{60}\text{Fe}$  in supernovae is discussed in detail by Limongi & Chieffi (2006), where the neutron density reached during the shock is identified as a key parameter for the yield. Despite the increase in the density of free nucleons due to neutrino spallation reactions, we find no significant modification of the  $^{60}\text{Fe}$  yield because neutrons are mostly captured by other, in particular heavier nuclei.

## 6. CONCLUSIONS

We have performed an updated study of  $\nu$  process nucleosynthesis taking into account for the first time the results from recent supernova simulations (Hüdepohl et al. 2010; Martínez-Pinedo et al. 2012; Martínez-Pinedo et al. 2014) that predict noticeably lower average energies particularly for  $\mu$  and  $\tau$  (anti)neutrinos. As a result we found charged current processes to be now more relevant. Compared to previous



studies, we use a full set of neutrino-induced charged- and neutral current reactions including spallation products for all nuclei in our reaction network with charge numbers  $Z < 76$ . Where cross sections derived from experimental data or dedicated shell model calculations are available we use those and we have included additional experimental data to infer the low energy part of cross sections for several charged current processes. This extensive compilation of cross sections for neutrino induced reactions will be published along with this article and can then be employed for the calculation of the next generation of stellar yield tables.

We have performed this study for a range of progenitor models for massive stars with ZAMS masses in the range between 13 and 30  $M_{\odot}$ , highlighting sensitivities and trends with respect to stellar structure and composition. Our nucleosynthesis study confirms the contribution of the  $\nu$  process to the production of  $^{11}\text{B}$ ,  $^{138}\text{La}$ , and  $^{180}\text{Ta}$  and avoids the overproduction of these elements that has been found in previous studies. Furthermore, we discuss the interplay between  $\gamma$  process and  $\nu$  process production and find that for individual progenitor models, in particular for the 27  $M_{\odot}$  model, neutral current neutrino interactions leading to the emission of neutrons have a major effect on the production of  $^{180}\text{Ta}$  for some progenitor models.

We confirm that the  $\nu$  process cannot be the primary origin of  $^{19}\text{F}$  and emphasize remaining uncertainties with respect to thermonuclear reaction cross-sections and stellar structure. Moreover, we find that there is no nucleus for which the  $\nu$  process can be assumed as the only origin. Unless all other contributions to the solar inventory are well understood it is therefore near impossible to use comparisons to the solar abundances to give stringent constraints on neutrino properties. If we consider the scenario of a nearby supernova explosion polluting the pre-solar cloud with short-lived radioactive nuclei, we find that the  $^{36}\text{Cl}/^{35}\text{Cl}$  ratio that can be measured in meteoritic grains is sensitive to the  $\bar{\nu}_e$  neutrino spectra. In this case, the  $^{36}\text{Cl}/^{35}\text{Cl}$  ratio could be used as a “neutrino thermometer”.

Including neutrino reactions with on all nuclei in our network we have identified effects on nuclei on the 10% level that have not been discussed before in the literature, including the p-nucleus  $^{113}\text{In}$ . We also find modifications of the yields of  $^{33}\text{S}$ ,  $^{40}\text{Ar}$ ,  $^{41}\text{K}$  and Fe-group nuclei that originate from the Si/O shell. Quantitatively, those results need to be taken with caution due to the limits of our 1D supernova model. We also have included reactions suggested by Heger et al. (2005) and find their effects to be small. We conclude that for the range of supernova models the most important effects of the  $\nu$  process on the production of stable nuclei have been identified. In the second part we discuss how neutrino-induced reactions, directly and indirectly, contribute to the production of long- and short-lived radioactive nuclei. For  $^{92}\text{Nb}$  and  $^{98}\text{Tc}$  we also discuss the competition thermonuclear and neutrino induced production. Within our model we cannot explain the  $^{92}\text{Nb}/^{93}\text{Nb}$  ratio found in meteoritic grains but due to the sensitivity of the yields to nuclear reaction rates and stellar structure and potential contribution from neutrino driven winds further studies are required.

The yields of  $^{22}\text{Na}$  and  $^{26}\text{Al}$ , both prime candidates for gamma-ray astronomy, are enhanced. For  $^{26}\text{Al}$  the magnitude of this enhancement is of the order of a few %. We also find that significantly larger uncertainties due to nuclear reaction rates remain. Even though the enhancement of the production of  $^{22}\text{Na}$  is of the order of 50% we do not expect a direct effect

on the supernova lightcurve and we estimate that the fluxes of characteristic  $\gamma$  ray emission are below the limit of the sensitivity of current instruments. However, the production of  $^{22}\text{Na}$  in the O/C leads us to suggest the  $\nu$  process as the origin of the Ne-E(L) component found in low density graphite grains.

Many of the relevant neutrino-nucleus cross-sections rely almost entirely on theoretical calculations and are therefore accompanied by large uncertainties. Experimental data on the relevant transitions could help to reduce the uncertainties in order to make inferences from observations more reliable. Furthermore, important uncertainties remain related to the progenitor structure (Woosley et al. 2002), helium burning rates (Austin et al. 2014), and the long term evolution of the neutrino spectra and neutrino oscillations (Wu et al. 2015).

We thank Yong-Zhong Qian, Projjwal Banerjee and Meng-Ru Wu for useful discussions. This work was partly supported by the Deutsche Forschungsgemeinschaft through contract SFB 1245 and the Helmholtz Association through the Nuclear Astrophysics Virtual Institute (VH-VI-417). AH was supported by an Australian Research Council (ARC) Future Fellowship (FT120100363) and by the US National Science Foundation under Grant No. PHY-1430152 (JINA Center for the Evolution of the Elements).

## REFERENCES

- Amari, S., 2009, *ApJ*, 690, 1424  
 Amari, S., Hoppe, P., Zinner, E., & Lewis, R. S., 1992, *ApJ*, 394, L43  
 Anderson, B. D., Tamimi, N., Baldwin, A. R., Elaasar, M., Mader, R., Manley, D. M., Mostajabodda’vati, M., Watson, J. W., Zhang, W. M., & Foster, C. C., 1991, *Phys. Rev. C*, 43, 50  
 Angulo, C., Arnould, M., Rayet, M., Descouvemont, P., Baye, D., Leclercq-Willain, C., Coc, A., Barhoumi, S., Aguer, P., Rolfs, C., et al., 1999, *NuPhA*, 656, 3  
 Arnould, M., & Takahashi, K., 1999, *Rep. Prog. Phys.*, 62, 395  
 Asplund, M., Grevesse, N., Sauval, A. J., & Scott, P., 2009, *ARA&A*, 47, 481  
 Austin, S. M., West, C., & Heger, A., 2014, *Phys. Rev. Lett.*, 112, 111101  
 Balasi, K. G., Langanke, K., & Martínez-Pinedo, G., 2015, *Progress in Particle and Nuclear Physics*, 85, 33  
 Banerjee, P., Qian, Y.-Z., Heger, A., & Haxton, W. C., 2016, *Nature Communications*, 7, 13639  
 Becker, H., & Walker, R. J., 2003, *Nature*, 425, 152  
 Belic, D., Arlandini, C., Besserer, J., de Boer, J., Carroll, J. J., Enders, J., Hartmann, T., Käppeler, F., Kaiser, H., Kneissl, U., et al., 2002, *Phys. Rev. C*, 65, 035801  
 Black, D., & Pepin, R., 1969, *Earth and Planetary Science Letters*, 6, 395  
 Brown, B. A., & Richter, W. A., 2006, *Phys. Rev. C*, 74, 034315  
 Burbidge, E. M., Burbidge, G. R., Fowler, W. A., & Hoyle, F., 1957, *Rev. Mod. Phys.*, 29, 547  
 Byelikov, A., Adachi, T., Fujita, H., Fujita, K., Fujita, Y., Hatanaka, K., Heger, A., Kalmykov, Y., Kawase, K., Langanke, K., et al., 2007, *Phys. Rev. Lett.*, 98, 082501  
 Cameron, A. G. W., 1957, *PASP*, 69, 201  
 Caughlan, G. R., & Fowler, W. A., 1988, *At. Data Nucl. Data Tables*, 40, 283  
 Caurier, E., Langanke, K., Martínez-Pinedo, G., & Nowacki, F., 1999, *NuPhA*, 653, 439  
 Cheoun, M.-K., Ha, E., Hayakawa, T., Chiba, S., Nakamura, K., Kajino, T., & Mathews, G. J., 2012, *Phys. Rev. C*, 85, 065807  
 Clayton, D. D., 1975, *Nature*, 257, 36  
 Clayton, D. D., Liu, W., & Dalgarno, A., 1999, *Science*, 283, 1290  
 Cyburt, R. H., Amthor, A. M., Ferguson, R., Meisel, Z., Smith, K., Warren, S., Heger, A., Hoffman, R. D., Rauscher, T., Sakharuk, A., et al., 2010, *ApJS*, 189, 240  
 Dauphas, N., & Chaussidon, M., 2011, *Annual Review of Earth and Planetary Sciences*, 39, 351  
 Dauphas, N., Marty, B., & Reisberg, L., 2002, *ApJ*, 565, 640  
 Diehl, R., 2013, *Astron. Rev.*, 8, 19  
 Diehl, R., Hallöin, H., Kretschmer, K., Lichti, G. G., Schönfelder, V., Strong, A. W., von Kienlin, A., Wang, W., Jean, P., Knödseder, J., et al., 2006, *Nature*, 439, 45  
 Diehl, R., & Timmes, F. X., 1998, *PASP*, 110, 637  
 Dillmann, I., Szücs, T., Plag, R., Fülöp, Z., Käppeler, F., Mengoni, A., & Rauscher, T., 2014, *Nuclear Data Sheets*, 120, 171  
 Domogatskii, G. V., & Nadezhin, D. K., 1980, *Ap&SS*, 70, 33

- Ertl, T., Janka, H.-T., Woosley, S. E., Sukhbold, T., & Ugliano, M., 2016, *ApJ*, 818, 124
- Fischer, T., Whitehouse, S. C., Mezzacappa, A., Thielemann, F.-K., & Liebendörfer, M., 2009, *A&A*, 499, 1
- Fischer, T., Whitehouse, S. C., Mezzacappa, A., Thielemann, F.-K., & Liebendörfer, M., 2010, *A&A*, 517, A80
- Fuller, G. M., Fowler, W. A., & Newman, M. J., 1982, *ApJS*, 48, 279
- Fuller, G. M., & Meyer, B. S., 1995, *ApJ*, 453, 792
- Gazit, D., & Barnea, N., 2007, *Phys. Rev. Lett.*, 98, 192501
- Grawe, H., Langanke, K., & Martínez-Pinedo, G., 2007, *Rep. Prog. Phys.*, 70, 1525
- Grefenstette, B. W., Harrison, F. A., Boggs, S. E., Reynolds, S. P., Fryer, C. L., Madsen, K. K., Wik, D. R., Zoglauer, A., Ellinger, C. I., Alexander, D. M., et al., 2014, *Nature*, 506, 339
- Hayakawa, T., Nakamura, K., Kajino, T., Chiba, S., Iwamoto, N., Cheoun, M. K., & Mathews, G. J., 2013, *ApJ*, 779, L9
- Heger, A., Kolbe, E., Haxton, W., Langanke, K., Martínez-Pinedo, G., & Woosley, S. E., 2005, *Phys. Lett. B*, 606, 258
- Hoffman, R. D., Woosley, S. E., Fuller, G. M., & Meyer, B. S., 1996, *ApJ*, 460, 478
- Horiuchi, S., Nakamura, K., Takiwaki, T., Kotake, K., & Tanaka, M., 2014, *MNRAS*, 445, L99
- Hüdepohl, L., Müller, B., Janka, H., Marek, A., & Raffelt, G. G., 2010, *Phys. Rev. Lett.*, 104, 251101
- Huss, G. R., Meyer, B. S., Srinivasan, G., Goswami, J. N., & Sahijpal, S., 2009, *Geochim. Cosmochim. Acta*, 73, 4922
- Iliadis, C., Champagne, A., Chieffi, A., & Limongi, M., 2011, *ApJS*, 193, 16
- Iliadis, C., D'Auria, J. M., Starrfield, S., Thompson, W. J., & Wiescher, M., 2001, *ApJS*, 134, 151
- Iliadis, C., Longland, R., Champagne, A. E., Coc, A., & Fitzgerald, R., 2010, *NuPhA*, 841, 31
- Iyudin, A. F., 2010, *Astronomy Reports*, 54, 611
- Iyudin, A. F., Diehl, R., Bloemen, H., Hermsen, W., Lichti, G. G., Morris, D., Ryan, J., Schönfelder, V., Steinle, H., Varendorff, M., et al., 1994, *A&A*, 284, L1
- Jacobsen, B., Matzel, J., Hutcheon, I. D., Krot, A. N., Yin, Q.-Z., Nagashima, K., Ramon, E. C., Weber, P. K., Ishii, H. A., & Ciesla, F. J., 2011, *ApJ*, 731, L28
- Jacobsen, B., Matzel, J., Hutcheon, I. D., Ramon, E., Krot, A. N., Ishii, H. A., Nagashima, K., & Yin, Q.-Z., 2009, in *Lunar and Planetary Science Conference*, volume 40 of *Lunar and Planetary Science Conference*, p. 2553
- Jönsson, H., Ryde, N., Spitoni, E., Matteucci, F., Cunha, K., Smith, V., Hinkle, K., & Schultheis, M., 2017, *ApJ*, 835, 50
- Käppeler, F., Arlandini, C., Heil, M., Voss, F., Wisshak, K., Reifarther, R., Straniero, O., Gallino, R., Masera, S., & Travaglio, C., 2004, *Phys. Rev. C*, 69, 055802
- Kelić, A., Valentina Ricciardi, M., & Schmidt, K.-H., 2009, *ArXiv e-prints*, 0906.4193
- Kheswa, B. V., Wiedeking, M., Giacoppo, F., Gorieli, S., Guttormsen, M., Larsen, A. C., Bello Garrote, F. L., Eriksen, T. K., Gørgen, A., Hagen, T. W., et al., 2015, *Physics Letters B*, 744, 268
- Kiss, G. G., Mohr, P., Fülöp, Z., Rauscher, T., Gyürky, G., Sztücs, T., Halász, Z., Somorjai, E., Ornelas, A., Yalçın, C., et al., 2013, *Phys. Rev. C*, 88, 045804
- Kobayashi, C., Izutani, N., Karakas, A. I., Yoshida, T., Yong, D., & Umeda, H., 2011, *ApJ*, 739, L57
- Kolbe, E., Langanke, K., Krewald, S., & Thielemann, F.-K., 1992, *NuPhA*, 540, 599
- Kolbe, E., Langanke, K., Martínez-Pinedo, G., & Vogel, P., 2003, *J. Phys. G: Nucl. Part. Phys.*, 29, 2569
- Kozma, C., & Fransson, C., 1998, *ApJ*, 496, 946
- Langanke, K., & Martínez-Pinedo, G., 2003, *Rev. Mod. Phys.*, 75, 819
- Langanke, K., & Schatz, H., 2013, *Phys. Scr.*, T152, 014011
- Lattimer, J. M., Schramm, D. N., & Grossman, L., 1978, *ApJ*, 219, 230
- Limongi, M., & Chieffi, A., 2006, *ApJ*, 647, 483
- Lin, Y., Guan, Y., Leshin, L. A., Ouyang, Z., & Wang, D., 2005, *Proceedings of the National Academy of Science*, 102, 1306
- Lodders, K., 2003, *ApJ*, 591, 1220
- Loens, H. P., 2010, *Microscopic radiative strength functions and fission barriers for r-process nucleosynthesis*, Ph.D. thesis, TU Darmstadt
- Martínez-Pinedo, G., Fischer, T., & Huther, L., 2014, *J. Phys. G: Nucl. Part. Phys.*, 41, 044008
- Martínez-Pinedo, G., Fischer, T., Lohs, A., & Huther, L., 2012, *Phys. Rev. Lett.*, 109, 251104
- McKeegan, K. D., & Davis, A. M., 2003, *Treatise on Geochemistry*, 1, 711
- Meier, M. M. M., Heck, P. R., Amari, S., Baur, H., & Wieler, R., 2012, *Geochim. Cosmochim. Acta*, 76, 147
- Mirizzi, A., Tamborra, I., Janka, H.-T., Saviano, N., Scholberg, K., Bollig, R., Hüdepohl, L., & Chakraborty, S., 2016, *Riv. del Nuovo Cim.*, 39, 1
- Mohr, P., 2016, *Phys. Rev. C*, 93, 065804
- Mohr, P., Käppeler, F., & Gallino, R., 2007, *Phys. Rev. C*, 75, 012802
- Müller, B., Heger, A., Liptai, D., & Cameron, J. B., 2016, *MNRAS*, 460, 742
- Murty, S. V. S., Goswami, J. N., & Shukolyukov, Y. A., 1997, *ApJ*, 475, L65
- O'Connor, E., & Ott, C. D., 2011, *ApJ*, 730, 70
- Prantzos, N., 2007, *Space Sci. Rev.*, 130, 27
- , 2012, *A&A*, 542, A67
- Rauscher, T., Heger, A., Hoffman, R. D., & Woosley, S. E., 2002, *ApJ*, 576, 323
- Rauscher, T., & Thielemann, F.-K., 2000, *At. Data Nucl. Data Tables*, 75, 1
- Renda, A., Fenner, Y., Gibson, B. K., Karakas, A. I., Lattanzio, J. C., Campbell, S., Chieffi, A., Cunha, K., & Smith, V. V., 2004, *MNRAS*, 354, 575
- Roig, O., Jandel, M., Méot, V., Bond, E. M., Bredeweg, T. A., Couture, A. J., Haight, R. C., Keksis, A. L., Rundberg, R. S., Ullmann, J. L., et al., 2016, *Phys. Rev. C*, 93, 034602
- Sbordone, L., Bonifacio, P., Caffau, E., Ludwig, H.-G., Behara, N. T., González Hernández, J. I., Steffen, M., Cayrel, R., Freytag, B., van't Veer, C., et al., 2010, *A&A*, 522, A26
- Schönbächler, M., Rehkämper, M., Halliday, A. N., Lee, D.-C., Bourton-Denise, M., Zanda, B., Hattendorf, B., & Günther, D., 2002, *Science*, 295, 1705
- Spite, F., & Spite, M., 1982, *A&A*, 115, 357
- Sukhbold, T., Woosley, S., & Heger, A., 2017, *ArXiv e-prints*, 1710.03243
- Sukhbold, T., & Woosley, S. E., 2014, *ApJ*, 783, 10
- Suwa, Y., & Müller, E., 2016, *MNRAS*, 460, 2664
- Takigawa, A., Miki, J., Tachibana, S., Huss, G. R., Tominaga, N., Umeda, H., & Nomoto, K., 2008, *ApJ*, 688, 1382-1387
- Tatischeff, V., Tavani, M., von Ballmoos, P., Hanlon, L., Oberlack, U., Aboudan, A., Argan, A., Bernard, D., Brogna, A., Bulgarelli, A., et al., 2016, in *Space Telescopes and Instrumentation 2016: Ultraviolet to Gamma Ray*, volume 9905 of *Proc. SPIE*, p. 99052N
- Teegarden, B. J., & Watanabe, K., 2006, *ApJ*, 646, 965
- Thielemann, F.-K., Arcones, A., Käppeli, R., Liebendörfer, M., Rauscher, T., Winteler, C., Fröhlich, C., Dillmann, I., Fischer, T., Martínez-Pinedo, G., et al., 2011, *PrPNP*, 66, 346
- Timmes, F. X., Woosley, S. E., Hartmann, D. H., Hoffman, R. D., Weaver, T. A., & Matteucci, F., 1995, *ApJ*, 449, 204
- Travaglio, C., Röpke, F. K., Gallino, R., & Hillebrandt, W., 2011, *ApJ*, 739, 93
- Ugliano, M., Janka, H.-T., Marek, A., & Arcones, A., 2012, *ApJ*, 757, 69
- Wasserburg, G. J., Busso, M., Gallino, R., & Nollett, K. M., 2006, *NuPhA*, 777, 5
- Weaver, T. A., Zimmerman, G. B., & Woosley, S. E., 1978, *ApJ*, 225, 1021
- Wiescher, M., Käppeler, F., & Langanke, K., 2012, *ARA&A*, 50, 165
- Winkler, C., Diehl, R., Ubertini, P., & Wilms, J., 2011, *Space Sci. Rev.*, 161, 149
- Wisshak, K., Voss, F., Arlandini, C., Bečvář, F., Straniero, O., Gallino, R., Heil, M., Käppeler, F., Krčička, M., Masera, S., et al., 2001, *Physical Review Letters*, 87, 251102
- Wongwathanarat, A., Janka, H.-T., Müller, E., Pllumbi, E., & Wanajo, S., 2017, *ApJ*, 842, 13
- Woosley, S. E., Hartmann, D., & Pinto, P. A., 1989, *ApJ*, 346, 395
- Woosley, S. E., Hartmann, D. H., Hoffman, R. D., & Haxton, W. C., 1990, *ApJ*, 356, 272
- Woosley, S. E., Heger, A., & Weaver, T. A., 2002, *Rev. Mod. Phys.*, 74, 1015
- Woosley, S. E., & Weaver, T. A., 1995, *ApJS*, 101, 181
- Wu, M.-R., Qian, Y.-Z., Martínez-Pinedo, G., Fischer, T., & Huther, L., 2015, *Phys. Rev. D*, 91, 065016
- Yoshida, T., Kajino, T., & Hartmann, D. H., 2005, *Phys. Rev. Lett.*, 94, 231101
- Young, P. A., & Fryer, C. L., 2007, *ApJ*, 664, 1033
- Zegers, R. G. T., Akimune, H., Austin, S. M., Bazin, D., van den Berg, A. M., Berg, G. P. A., Brown, B. A., Brown, J., Cole, A. L., Daito, I., et al., 2006, *Phys. Rev. C*, 74, 024309
- Zinner, E., 1998, *Annual Review of Earth and Planetary Sciences*, 26, 147